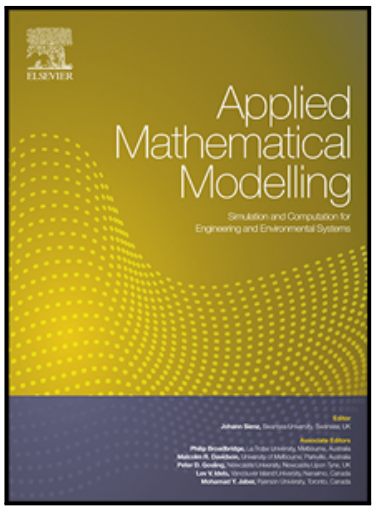

Dynamics of spinning pipes conveying flow with internal elliptical cross-section surrounded by an external annular fluid by considering rotary inertia effects

Ali Ebrahimi-Mamaghani , Omid Koochakianfard , Navid Mostoufi , Hamed Haddad Khodaparast

PII: S0307-904X(23)00140-3
DOI: https://doi.org/10.1016/j.apm.2023.03.043
Reference: APM 14977

To appear in: *Applied Mathematical Modelling*

Received date: 4 November 2022
Revised date: 17 February 2023
Accepted date: 30 March 2023

Please cite this article as: Ali Ebrahimi-Mamaghani , Omid Koochakianfard , Navid Mostoufi , Hamed Haddad Khodaparast , Dynamics of spinning pipes conveying flow with internal elliptical cross-section surrounded by an external annular fluid by considering rotary inertia effects, *Applied Mathematical Modelling* (2023), doi: https://doi.org/10.1016/j.apm.2023.03.043

Highlights

- Vibration of spinning pipes conveying flow submerged in an external annular fluid
- Non-uniformity of internal flow velocity distribution and rotary inertia effects
- Impacts of geometry, environment, stabilizer, gravity, external fluid mass ratio
- Divergence and flutter instabilities of the system with an asymmetric cross-section
- Campbell diagram, stability maps, and frequency analysis

Dynamics of spinning pipes conveying flow with internal elliptical cross-section surrounded by an external annular fluid by considering rotary inertia effects

Ali Ebrahimi-Mamaghani [a], Omid Koochakianfard [b], Navid Mostoufi [a,*] , Hamed Haddad Khodaparast [c]

[a] Multiphase Systems Research Lab, School of Chemical Engineering, College of Engineering, University of Tehran, Tehran 11155/4563, Iran

[b] Department of Mechanical Engineering, Tarbiat Modares University, Tehran, Iran

[c] College of Engineering, Swansea University, Bay Campus, Fabian Way, Crymlyn Burrows, Swansea SA1 8EN, United Kingdom

[*]Corresponding author. Tel.: +98 21 6696-7781; fax: +98 21 6645-7784.
E-mail addresses: a.ebrahimimamaghani@gmail.com, koochakianfardomid@modares.ac.ir, mostoufi@ut.ac.ir, h.haddadkhodaparast@swansea.ac.uk

Abstract

In this work, the vibration and stability of spinning pipes with an internal elliptical cross-section concurrently subjected to internal flow and external annular fluid are analyzed by considering rotary inertia effects and the non-uniformity of internal flow velocity distribution. To model the system, axial force, internal pressure, hygro-thermal loads, viscoelastic properties, and gravitational effects were incorporated. The coupled dynamic equations of transverse motions of the pipe were derived by exploiting the extended Hamilton's principle. With the aid of the Laplace transform and Galerkin discretization method, eigenvalues and stability conditions of the system were determined. Moreover, the divergence instability conditions of the system were acquired analytically. Then, the current investigation results were compared and verified with existing experimental and theoretical data in open literature. The impacts of key parameters, such as stabilizer characteristics, boundary conditions, geometrical features, and external fluid mass ratio, on the vibration frequencies and instability thresholds, were evaluated. It was concluded that, contrary to the internal circular cross-section case, the divergence instability region can be observed in the stability evaluation of the system with the internal elliptical cross-section. It was found that considering the rotary inertia effects reduces the critical velocities of the system. Also, the results showed that by increasing the stabilizer damping, the detached stable region is

detected in the stability map of cantilevered pipes. The present research results can be beneficial for the optimal design of industrial equipment such as drill string pipes.

Keywords: Vibration and stability, pipe with internal elliptical cross-section, flow velocity modification factor, rotary inertia effects, stabilizer

1. Introduction

Flow-conveying pipes with unique dynamic characteristics have attracted the attention of multitudinous researchers in the last century [1-3]. In this regard, numerous scientific studies have been dedicated to identifying the fluid-structure interaction (FSI) in these engineering systems [4-7]. Comprehensive reviews on mathematical simulation and vibration analysis of flow-carrying pipes can be found in [8, 9]. Theoretical and experimental investigations have proved that due to the internal flow movement, divergence and flutter instabilities are perceived in the stability evaluation of pipes with diverse boundary conditions [10]. Also, due to the extensive capabilities of piping systems in the industry, engineers utilize them in complex environmental conditions such as humid and thermal fields [11, 12]. Within this context, Qian et al. [13] focused on the stability behavior of simply supported pipes transporting flow exposed to thermal loads by considering linear and nonlinear thermo-elastic relations. They used the differential quadrature method to estimate the stability margins of the pipe. Reddy et al. [14] modeled the nonlinear vibration of inclined functionally graded pipes containing pulsating hot flow. They surveyed the effects of temperature rise, flow velocity, and pipe inclination on the dynamic characteristics of the system. Esfahani et al. [15] developed a novel 3D-numerical model to analyze the vibration frequency of micropillars by considering the viscoelastic effects, hydrodynamic forces, and acoustic pressures. The effect of flow inertia on the vibration frequency was analyzed by Ji et al. [16] utilizing a microfluidic embedded quartz crystal microbalance device. Another common operating condition of pipes is when these practical structures are subjected to an external fluid [17, 18]. For this reason, several efforts have been devoted to the hydro-elastic simulation of these applicable systems in the presence of an external fluid. For instance, Ni et al. [19] performed the frequency analysis of axially moving pipes carrying flow embedded in an external fluid. With the help of the Galerkin discretization method,

they inspected the effects of internal flow and external fluid mass ratios on the stability regions of supported systems. Huang et al. [20] addressed the vibration control of a pipe simultaneously subjected to axial internal and sinusoidal external flows by applying a nonlinear absorber. They investigated the effect of absorber characteristics on hydrodynamics, vibration reduction, and instability thresholds of the system by analyzing frequency-response curves, bifurcation diagrams, and phase plane trajectories. One of the interesting topics that has received less attention in the technical literature is the effects of the cross-section shape on the dynamic response and stability behavior of piping systems. From the engineering design point of view, pipes with non-circular sections, such as rectangular, elliptical, and triangular, could lead to performance improvement and an appealing appearance. Specifically, the elliptical cross-section has better local strength against impact loads than the typical circular cross-section due to its torsional rigidity [21]. Also, owning different bending stiffness about its principal axes, the elliptical cross-section has a higher bending capacity in various loading conditions than the conventional circular cross-section. In this field, Wang et al. [22] analyzed the lateral vibration of flow-carrying microscale pipes with different cross-sections. They disclosed that the centrifugal force of the system with a rectangular cross-section is less than that of the system with a square cross-section. Heshmati et al. [23] scrutinized the flow-induced oscillation of functionally graded pipes with an elliptical cross-section. They interpreted the effects of material gradation and geometric properties on the system dynamics.

Spinning pipes transporting flow have several applications in engineering industries such as ocean mining, turbomachinery, and heat exchangers. The combination of the gyroscopic effects of spinning motion and the FSI in these structures results in a novel paradigm of bi-gyroscopic systems [24]. Therefore, scientists have been encouraged to report the stability and dynamic essence of these structures in recent years. In this sense, Liang et al. [25] analyzed the nonlinear dynamics of flexible viscoelastic flow-carrying pipes with a spinning motion by applying analytical and numerical approaches. They explored the effects of variations in internal flow velocity and spin speed on the vibration behavior of the structure. Bahaldini and Saidi [26] discussed the thermo-mechanical behavior of spinning pipes reinforced with carbon nanotubes. They studied the effect of various carbon nanotube distributions on the critical flow velocity of the system. Liang et al. [27] considered the free vibration of vertical spinning pipes carrying flow

with axial deployment. They calculated the time-dependent vibration frequencies and dynamic response of the system. Eftekhari and Hosseini [28] concentrated on the stability of spinning thin-walled graded flow-conveying pipes in thermal conditions. They reported the contributions of the volume fraction of graded materials and axial compressive force in the stability borders of the system. Liang et al. [29] developed a three-dimensional mathematical model for the dynamics of spinning fluid-filled pipes surrounded by an external annular flow. They reflected the effects of external viscous flow and gravity on the dynamic response and vibration frequencies of the system. According to the technical literature, it can be found that the majority of the available studies in this field are based on the Euler-Bernoulli theory assumptions. In this theory, only transverse deflection is considered for the system, and the cross-section rotation of the system after the deformation (i.e., rotary inertia effects for the pipe and internal flow) is ignored.

In the present investigation, a detailed mathematical model is established for spinning viscoelastic pipes conveying internal flow with an internal elliptical cross-section (asymmetric but axisymmetric cross-section) immersed in an annular external fluid domain, including the rotary inertia effects and non-uniformity of the internal flow velocity profile. Also, parametric studies are accomplished to explain the impacts of gravity, internal pressure, axial tensile force, stabilizer, boundary conditions, external fluid mass ratio, hygro-thermal environments, and geometric characteristics on the vibration and stability of the system. The main novelties of the current research can be summarized as follows:

a) Examination of the effects of the asymmetric cross-section on the dynamics of bi-gyroscopic systems
b) Investigation of the impacts of the non-uniformity of internal flow velocity distribution on the vibration characteristics and stability threshold of spinning pipes
c) Consideration of the rotary inertia effects in mathematical modeling of doubly gyroscopic structures

In the following, first, the governing equations of the system motion are acquired based on Hamilton's principle. Then, vibration frequencies and instability thresholds of the system are computed by implementing the Laplace transform and Galerkin discretization procedure. Also,

an analytical approach is proposed to recognize the static instability of the submerged pipe containing flow. Finally, the effects of different system parameters on the system dynamics are assessed and revealed.

2. Problem formulation

Figure 1(a) depicts the geometric configuration of a flexible spinning cantilevered pipe conveying incompressible flow. The cross-section of the considered system is also shown in Figure 1 (b). The major and minor semi-axes of the internal elliptical cross-section of the pipe are denoted by b and a, respectively. The length of the pipe is L, and the diameter of the external cross-section of the pipe is D_P. It is assumed that the pipe rotates with constant spin speed Ω and transmits the internal flow with the constant axial velocity U. The considered pipe is immersed in an annular fluid medium. The diameter of the surrounding fluid domain is D_{ch}. Also, it is supposed that a concentrated stabilizer consists of a spring with the stiffness of $K_{stab,}$ and a damper with a damping coefficient of C_{stab} is installed at the distance x_{stab} from the upstream end.

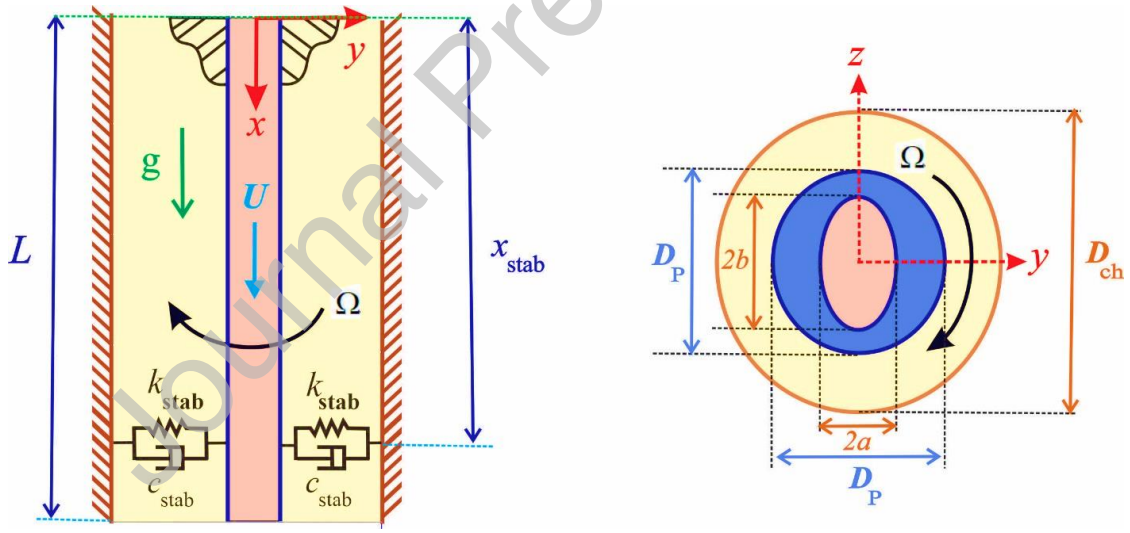

(a) (b)

Fig. 1. Schematic view of a spinning cantilevered pipe containing flow immersed in an external annular medium attached to the stabilizer (b) cross-section of the considered system

The position vector of an arbitrary point of the deformed pipe is expressed as follows [30]:

$$\mathbf{r} = (x + u - yv' - zw')\mathbf{i} + (y + v)\mathbf{j} + (z + w)\mathbf{k} \quad (1)$$

in which **i**, **j**, and **k** are the unit vectors in the *x*, *y*, and *z* directions, respectively. Also, *u*, *v*, and *w* are the lateral displacements along the *x*, *y*, and *z* directions. In addition, the prime notation demonstrates the derivative with respect to *x*. It should be mentioned that in the present model, transverse motion and cross-section rotation of the pipe are considered. As a result, this model presents a better approximation of the vibration frequencies of the system than the Euler-Bernoulli model. Also, compared with the Timoshenko model, this model does not consider the shear deformation effects in the system.

The lateral coordinates, i.e., *y* and *z*, are time-dependent functions, and their temporal derivatives are given by $\frac{\partial y}{\partial t} = -z\Omega$ and $\frac{\partial z}{\partial t} = y\Omega$. As a result, the velocity vector of the pipe can be computed as follows [31, 32]:

$$\mathbf{v}_{\mathrm{P}} = \dot{\mathbf{r}} + \boldsymbol{\Omega} \times \mathbf{r} = (\dot{u} + \Omega z v' - y\dot{v}' - \Omega y w' - z\dot{w}')\mathbf{i} + (\dot{v} - \Omega w)\mathbf{j} + (\dot{w} + \Omega v)\mathbf{k} \quad (2)$$

where the dot notation denotes the temporal derivative.

The velocity vector of the center of an internal flow element can be expressed as follows [33, 34]:

$$\mathbf{v}_{\mathrm{f}} = \mathbf{v}_{\mathrm{P}} + U\boldsymbol{\tau} \quad (3)$$

in which $\boldsymbol{\tau}$ is the unit vector tangential to the pipe and is computed as follows:

$$\boldsymbol{\tau} = \mathbf{r}' = (1 + u' - yv'' - zw'')\mathbf{i} + v'\mathbf{j} + w'\mathbf{k} \quad (4)$$

It should be noted that according to Eq. (3), it can be found that the radial velocity of the internal flow is equal to the instantaneous velocity of the pipe, which this situation satisfies the impermeability boundary conditions of the pipe wall [35].

The total kinetic energy of the system, including the kinetic energies of the pipe and the internal flow, can be formulated as follows:

$$T_{\mathrm{tot}} = T_{\mathrm{P}} + T_{\mathrm{f}} = \frac{1}{2}\int_0^L \rho_{\mathrm{P}}(\mathbf{v}_{\mathrm{P}}.\mathbf{v}_{\mathrm{P}})A_{\mathrm{P}}\mathrm{d}x + \frac{1}{2}\int_0^L \rho_{\mathrm{f}}^{\mathrm{i}}(\mathbf{v}_{\mathrm{f}}.\mathbf{v}_{\mathrm{f}})A_{\mathrm{f}}\mathrm{d}x \quad (5)$$

where ρ_{P} and $\rho_{\mathrm{f}}^{\mathrm{i}}$ are the density of the pipe and internal flow, respectively. Besides, A_{P} and A_{f} are the external and internal cross-sections of the pipe. It should be mentioned that based on Eq. (5), it is assumed that at an arbitrary cross-section of the pipe, the internal flow velocity has a constant value, and the effect of the non-uniformity of the internal flow velocity distribution over the inner cross-sectional area of the pipe will be considered later.

By inserting Eqs. (2-4) into Eq. (5) and ignoring the nonlinear terms, the kinetic energy relations of the pipe and the internal flow are rewritten, respectively, as follows:

$$T_{\mathrm{P}} = \frac{1}{2}\rho_{\mathrm{P}} A_{\mathrm{P}}\left(\dot{v}^2 + \dot{w}^2 + \Omega^2(v^2 + w^2) - 2\Omega(\dot{v}w - v\dot{w})\right) + \frac{1}{2}\rho_{\mathrm{P}}\left(\Omega^2\left(I_{\mathrm{y}}^{\mathrm{P}} v'^2 + I_{\mathrm{z}}^{\mathrm{P}} w'^2\right) - 2\Omega\left(I_{\mathrm{y}}^{\mathrm{P}} v'\dot{w}' - I_{\mathrm{z}}^{\mathrm{P}} w'\dot{v}'\right) + I_{\mathrm{z}}^{\mathrm{P}}\dot{v}'^2 + I_{\mathrm{y}}^{\mathrm{P}}\dot{w}'^2\right) \tag{6}$$

$$\begin{aligned} T_{\mathrm{f}} = \frac{1}{2}\rho_{\mathrm{f}}^{\mathrm{i}} A_{\mathrm{f}}\Big(& U^2 + \dot{v}^2 + \dot{w}^2 + \Omega^2(v^2 + w^2) - 2\Omega(\dot{v}w - v\dot{w}) + U^2\left(v'^2 + w'^2\right) \\ & + 2U(\dot{v}v' + \dot{w}w') - 2\Omega U(wv' - vw')\Big) \\ & + \frac{1}{2}\rho_{\mathrm{f}}^{\mathrm{i}}\Big(I_{\mathrm{z}}^{\mathrm{f}}\dot{v}'^2 + I_{\mathrm{y}}^{\mathrm{f}}\dot{w}'^2 + \Omega^2\left(I_{\mathrm{y}}^{\mathrm{f}} v'^2 + I_{\mathrm{z}}^{\mathrm{f}} w'^2\right) + U^2\left(I_{\mathrm{z}}^{\mathrm{f}} v''^2 + I_{y}^{\mathrm{f}} w''^2\right) \\ & + 2U\left(I_{\mathrm{z}}^{\mathrm{f}} v''\dot{v}' + I_{\mathrm{y}}^{\mathrm{f}} w''\dot{w}'\right) - 2\Omega U\left(I_{\mathrm{y}}^{\mathrm{f}} v'w'' - I_{\mathrm{z}}^{\mathrm{f}} v''w'\right) - 2\Omega\left(I_{\mathrm{y}}^{\mathrm{f}} v'\dot{w}' + I_{\mathrm{z}}^{\mathrm{f}} w'\dot{v}'\right)\Big) \end{aligned} \tag{7}$$

in which $I_{\mathrm{y}}^{\mathrm{P}}$ and $I_{\mathrm{z}}^{\mathrm{P}}$ are the lateral area moments of the pipe, $I_{\mathrm{y}}^{\mathrm{f}}$ and $I_{\mathrm{y}}^{\mathrm{f}}$ are lateral area moments of inertial flow and can be defined by the following relations:

$$\left\{I_{\mathrm{y}}^{\mathrm{P}}, I_{\mathrm{z}}^{\mathrm{P}}\right\} = \rho_{\mathrm{P}} \int_{A_{\mathrm{P}}} \{z^2, y^2\}\mathrm{d}A_{\mathrm{P}} \tag{8}$$

$$\left\{I_{\mathrm{y}}^{\mathrm{f}}, I_{\mathrm{z}}^{\mathrm{f}}\right\} = \rho_{\mathrm{f}}^{\mathrm{i}} \int_{A_{\mathrm{f}}} \{z^2, y^2\}\mathrm{d}A_{\mathrm{f}} \tag{9}$$

It is necessary to mention that during the derivation of dynamic equations of the motion, the axial deformation of the pipe is ignored. This point can be justified by the feature that the axial displacement is negligible compared to the transverse displacements.

The bending strain potential energy of the system can be calculated according to the following expression [36, 37]:

$$V_{\mathrm{b}} = \frac{1}{2}\int_0^L \sigma_{\mathrm{x}}\varepsilon_{\mathrm{x}} A_{\mathrm{P}}\mathrm{d}x \tag{10}$$

where σ_{x} is the axial stress of the pipe.

It is noteworthy to consider the dissipation effects on the system dynamics. It is assumed that the internal dissipation of the system is appraised with the viscoelastic property of pipe materials. The Kelvin-Voigt viscoelastic model, which is a reliable two-parameter rheological model of

material, is adopted to assess the energy dissipation mechanism for the system as follows [38, 39]:

$$\sigma_{\mathrm{x}} = E\left(1 + \mu\frac{\partial}{\partial t}\right)\varepsilon_{\mathrm{x}} \tag{11}$$

in which E and μ are the elastic modulus and viscoelastic damping coefficient of the pipe, respectively. Also, ε_{x} is the axial strain of the pipe, and by ignoring the nonlinear effects, it can be stated for spinning systems as follows [40]:

$$\varepsilon_{\mathrm{x}} = -yv'' - zw'' \tag{12}$$

The strain energy induced by the hygro-thermal fields is also calculated as follows [41]:

$$V_{\mathrm{HT}} = \frac{1}{2}\int_0^L E(\alpha_{\mathrm{H}}\Delta H + \alpha_{\mathrm{T}}\Delta T)[(v')^2 + (w')^2]A_{\mathrm{P}}\mathrm{d}x \tag{13}$$

where α_{H} and α_{T} are the moisture and thermal expansion coefficients, ΔH and ΔT are the moisture and temperature gradients.

The potential energy generated by the stabilizer can be specified as follows [42]:

$$V_{\mathrm{stab}} = \frac{1}{2}[K_{\mathrm{stab}}(v^2 + w^2) + C_{\mathrm{stab}}(\dot{v}^2 + \dot{w}^2)]\delta_{\mathrm{dir}}(x - x_{\mathrm{stab}}) \tag{14}$$

where δ_{dir} is the Dirac delta function.

The gravitational potential energy of the system can be determined from the following relation [43]:

$$V_{\mathrm{g}} = \frac{1}{2}\left(\rho_{\mathrm{P}}A_{\mathrm{P}} + \rho_{\mathrm{f}}^{\mathrm{i}}A_{\mathrm{f}}\right)g\int_0^L (L - x)((v')^2 + (w')^2)\mathrm{d}x \tag{15}$$

where g is the gravitational acceleration.

The external work done by the axial tensile force, internal pressure, and the load exerted by the external fluid on the pipe can be acquired as follows [44-46]:

$$\delta W_{\mathrm{ex}} = -\int_0^L ([(P_{\mathrm{i}}A_{\mathrm{f}} - T)v'' + F_v]\delta v)\mathrm{d}x - \int_0^L ([(P_{\mathrm{i}}A_{\mathrm{f}} - T)w'' - T + F_w]\delta w)\mathrm{d}x \tag{16}$$

in which P_{i} is the internal flow pressure, and T is the applied tensile force to the pipe. Also, F_{v} and F_{w} are the transverse loads exerted on the pipe by the external fluid.

It is supposed that the external flow is continuously in contact with the pipe wall, and as a result, the cavitation and wake effects are neglected. Also, the amplitude oscillations of the pipe are small enough to be precisely modeled by linear formulations. Such small lateral deflections induce perturbations in the external fluid loading, and such perturbed loading can be determined by linearizing the Navier-Stokes equations. Abdollahi et al. [47] determined the steady-state external fluid loading according to the following relations:

$$F_v = -\frac{\pi}{4}\rho_{\mathrm{f}}^{\mathrm{e}} D_{\mathrm{P}}^2(\ddot{v} - 2\lambda\Omega\dot{w} - \Omega^2 v) \tag{17}$$

$$F_w = -\frac{\pi}{4}\rho_{\mathrm{f}}^{\mathrm{e}} D_{\mathrm{P}}^2(\ddot{w} + 2\lambda\Omega\dot{v} - \Omega^2 w) \tag{18}$$

where $\lambda = \frac{1}{1-\kappa^2}$. Also, $\kappa = \frac{D_{\mathrm{ch}}}{D_{\mathrm{P}}}$ is external to internal diameter ratio and $\rho_{\mathrm{f}}^{\mathrm{e}}$ is the external fluid density. It should be mentioned that the viscosity effect is supposed to exist only in the steady-state equations, which leads to a steady rotation of the external fluid.

The extended Hamilton's principle is utilized to achieve the governing equations of the motion of the pipe according to the following relation [48, 49]:

$$\delta_{\mathrm{var}} \int_{t_1}^{t_2} \left(T_{\mathrm{P}} + T_{\mathrm{f}} + W_{\mathrm{ex}} - V_{\mathrm{b}} - V_{\mathrm{HT}} - V_{\mathrm{stab}} - V_{\mathrm{g}} - \rho_{\mathrm{f}}^{\mathrm{i}} A_{\mathrm{f}} U(\dot{\mathbf{r}}_{\mathrm{L}} + U\tau_{\mathrm{L}})\delta_{\mathrm{var}}\mathbf{r}_{\mathrm{L}}\right)\mathrm{d}t = 0 \tag{19}$$

in which the index L refers to corresponding quantities at the end condition of the pipe.

By inserting the relations of kinetic and potential energies as well as the external work into Eq. (19), the partial differential equations of lateral motions are obtained as follows:

$$\begin{aligned}
&EI_{\mathrm{z}}^{\mathrm{P}}(v'''' + \mu\dot{v}'''') + \left(P_{\mathrm{i}}A_{\mathrm{f}} - T + E\alpha_{\mathrm{H}}A_{\mathrm{P}}\Delta H + E\alpha_{\mathrm{T}}A_{\mathrm{P}}\Delta T - \left(\rho_{\mathrm{P}}A_{\mathrm{P}} + \rho_{\mathrm{f}}^{\mathrm{i}}A_{\mathrm{f}}\right)g(L-x)\right)v'' \\
&\quad + \left(\rho_{\mathrm{P}}A_{\mathrm{P}} + \rho_{\mathrm{f}}^{\mathrm{i}}A_{\mathrm{f}}\right)gv' + (K_{\mathrm{stab}}v + C_{\mathrm{stab}}\dot{v})\delta_{\mathrm{dir}}(x - x_{\mathrm{stab}}) \\
&\quad + \frac{\pi}{4}\rho_{\mathrm{f}}^{\mathrm{e}} D_{\mathrm{P}}^2(\ddot{v} - 2\lambda\Omega\dot{w} - \Omega^2 v) + \left(\rho_{\mathrm{P}}A_{\mathrm{P}} + \rho_{\mathrm{f}}^{\mathrm{i}}A_{\mathrm{f}}\right)(\ddot{v} - 2\Omega\dot{w} - \Omega^2 v) \\
&\quad + \rho_{\mathrm{f}}^{\mathrm{i}}A_{\mathrm{f}}(U^2v'' + 2U\dot{v}' - 2U\Omega w') + \rho_{\mathrm{P}}\left(\Omega^2 I_{\mathrm{y}}^{\mathrm{P}}v'' - \Omega\left(I_{\mathrm{y}}^{\mathrm{P}} + I_{\mathrm{z}}^{\mathrm{P}}\right)\dot{w}'' - I_{\mathrm{z}}^{\mathrm{P}}\ddot{v}''\right) \\
&\quad + \rho_{\mathrm{f}}^{\mathrm{i}}\left(\Omega^2 I_{\mathrm{y}}^{\mathrm{f}}v'' - \Omega\left(I_{\mathrm{y}}^{\mathrm{f}} + I_{\mathrm{z}}^{\mathrm{f}}\right)\dot{w}'' - I_{\mathrm{z}}^{\mathrm{f}}\ddot{v}''\right) \\
&\quad - \rho_{\mathrm{f}}^{\mathrm{i}}\left(U^2 I_{\mathrm{z}}^{\mathrm{f}}v'''' + \Omega U\left(I_{\mathrm{y}}^{\mathrm{f}} + I_{\mathrm{z}}^{\mathrm{f}}\right)w''' + 2I_{\mathrm{z}}^{\mathrm{f}}U\dot{v}'''\right) = 0
\end{aligned} \tag{20}$$

$$
\begin{aligned}
&EI_{\mathrm{y}}^{\mathrm{P}}(w'''' + \mu\dot{w}'''') + \left(P_{\mathrm{i}}A_{\mathrm{f}} - T + E\alpha_{\mathrm{T}}A_{\mathrm{P}}\Delta T + E\alpha_{\mathrm{H}}A_{\mathrm{P}}\Delta H - \left(\rho_{\mathrm{P}}A_{\mathrm{P}} + \rho_{\mathrm{f}}^{\mathrm{i}}A_{\mathrm{f}}\right)g(L-x)\right)w'' \\
&\quad + \left(\rho_{\mathrm{P}}A_{\mathrm{P}} + \rho_{\mathrm{f}}^{\mathrm{i}}A_{\mathrm{f}}\right)gw' + (K_{\mathrm{stab}}w + C_{\mathrm{stab}}\dot{w})\delta_{\mathrm{dir}}(x - x_{\mathrm{stab}}) \\
&\quad + \frac{\pi}{4}\rho_{\mathrm{f}}^{\mathrm{e}}D_{\mathrm{P}}^{2}(\ddot{w} + 2\lambda\Omega\dot{v} - \Omega^{2}w) + \left(\rho_{\mathrm{P}}A_{\mathrm{P}} + \rho_{\mathrm{f}}^{\mathrm{i}}A_{\mathrm{f}}\right)(\ddot{w} + 2\Omega\dot{v} - \Omega^{2}w) \\
&\quad + \rho_{\mathrm{f}}^{\mathrm{i}}A_{\mathrm{f}}(U^{2}w'' + 2U\dot{w}' + 2U\Omega v') + \rho_{\mathrm{P}}\left(\Omega^{2}I_{\mathrm{z}}^{\mathrm{P}}w'' + \Omega\left(I_{\mathrm{y}}^{\mathrm{P}} + I_{\mathrm{z}}^{\mathrm{P}}\right)\dot{w}'' - I_{\mathrm{y}}^{\mathrm{P}}\ddot{w}''\right) \\
&\quad + \rho_{\mathrm{f}}^{\mathrm{i}}\left(\Omega^{2}I_{\mathrm{z}}^{\mathrm{f}}w'' + \Omega\left(I_{\mathrm{y}}^{\mathrm{f}} + I_{\mathrm{z}}^{\mathrm{f}}\right)\dot{v}'' - I_{y}^{\mathrm{f}}\ddot{w}''\right) \\
&\quad - \rho_{\mathrm{f}}^{\mathrm{i}}\left(U^{2}I_{y}^{\mathrm{f}}w'''' - \Omega U\left(I_{\mathrm{y}}^{\mathrm{f}} + I_{\mathrm{z}}^{\mathrm{f}}\right)v''' + 2I_{\mathrm{y}}^{\mathrm{f}}U\dot{w}'''\right) = 0
\end{aligned}
\tag{21}
$$

Similar to the majority of available studies in the field of mathematical modeling of pipes conveying fluid, the derived structural dynamic equations are based on the assumptions of plug flow (ideal flow). In this situation, it is supposed that the internal flow has a uniform velocity distribution over the internal cross-section of the pipe. It should be mentioned that this condition differs from fully developed turbulent flow (with a high Reynolds number) or laminar flow (with a low Reynolds number) [50]. As a result, the assumption of the plug flow condition for the internal flow of pipes is not realistic. In practice, if a non-uniform velocity distribution for the internal flow is considered, the resultant flow-related terms due to the internal flow should be recalculated. Flow velocity profiles for circular and elliptical cross-sections are considered according to the following relations, respectively [23]:

$$U(r) = 2\overline{U}\left(1 - \left(\frac{r}{R}\right)^{2}\right) \tag{22}$$

$$U(y,z) = 2\overline{U}\left(1 - \left(\frac{y}{a}\right)^{2} - \left(\frac{z}{b}\right)^{2}\right) \tag{23}$$

where $\overline{U}$ is the mean flow velocity across the pipe cross-section. Also, r and R are the distance from the cross-section center of the circular pipe and the radius of the internal cross-section of the pipe, respectively.

To determine the modification factors for the induced forces by the internal flow, including the Coriolis force, centrifugal load, and bi-gyroscopic effects due to FSI, by considering the non-

uniform velocity distribution profile for each differential element of the internal flow and integrating over the pipe cross-section, one can write:

For Coriolis forces:

$$\chi_1 = \frac{\int_{A_\mathrm{f}} \rho_\mathrm{f} U \mathrm{d}A_\mathrm{f}}{\rho_\mathrm{f} A_\mathrm{f} \bar{U}} = 1 \tag{24}$$

$$\chi_3 = \frac{\int_{A_\mathrm{f}} \rho_\mathrm{f} U y^2 \mathrm{d}A_\mathrm{f}}{\rho_\mathrm{f} \bar{U} I_\mathrm{f}^\mathrm{z}} = \frac{\int_{A_\mathrm{f}} \rho_\mathrm{f} U z^2 \mathrm{d}A_\mathrm{f}}{\rho_\mathrm{f} A_\mathrm{f} \bar{U} I_\mathrm{f}^\mathrm{y}} = \frac{2}{3} \tag{25}$$

For centrifugal loads:

$$\chi_2 = \frac{\int_{A_\mathrm{f}} \rho_\mathrm{f} U^2 \mathrm{d}A_\mathrm{f}}{\rho_\mathrm{f} A_\mathrm{f} \bar{U}^2} = \frac{4}{3} \tag{26}$$

$$\chi_4 = \frac{\int_{A_\mathrm{f}} \rho_\mathrm{f} U^2 y^2 \mathrm{d}A_\mathrm{f}}{\rho_\mathrm{f} \bar{U}^2 I_\mathrm{f}^\mathrm{z}} = \frac{\int_{A_\mathrm{f}} \rho_\mathrm{f} U^2 z^2 \mathrm{d}A_\mathrm{f}}{\rho_\mathrm{f} \bar{U}^2 I_\mathrm{f}^\mathrm{y}} = \frac{2}{3} \tag{27}$$

For bi-gyroscopic effects:

$$\chi_1 = \frac{\int_{A_\mathrm{f}} \rho_\mathrm{f} \Omega U \mathrm{d}A_\mathrm{f}}{\rho_\mathrm{f} \Omega \bar{U} A_\mathrm{f}} = 1 \tag{28}$$

$$\chi_3 = \frac{\int_{A_\mathrm{f}} \rho_\mathrm{f} U y^2 \mathrm{d}A_\mathrm{f}}{\rho_\mathrm{f} \bar{U} I_\mathrm{f}^\mathrm{z}} = \frac{\int_{A_\mathrm{f}} \rho_\mathrm{f} \Omega U z^2 \mathrm{d}A_\mathrm{f}}{\rho_\mathrm{f} \Omega \bar{U} A_\mathrm{f} I_\mathrm{f}^\mathrm{y}} = \frac{2}{3} \tag{29}$$

It should be noted that although the flow velocity profiles of circular and elliptical cross-sections are different, their modification factors are the same. Also, according to the results of Ref. [50], it can be deduced that the variations of the Reynolds number in the turbulent flow regime have a small effect on the modification factors. As a result, the aforementioned modification factors also give acceptable accuracy for the turbulent flow regime.

Also, the following dimensionless parameters are introduced to extract the non-dimensional dynamic equations:

$$(x^*, v^*, w^*, x^*_{\mathrm{stab}}) = \frac{(x, v, w, x_{\mathrm{stab}})}{L}\,, \qquad t^* = \frac{t}{L^2}\sqrt{\frac{E\sqrt{I^{\mathrm{P}}_{\mathrm{y}} I^{\mathrm{P}}_{\mathrm{z}}}}{\rho_{\mathrm{P}} A_{\mathrm{P}} + \rho^{\mathrm{i}}_{\mathrm{f}} A_{\mathrm{f}}}}\,, \qquad \Omega^* = \Omega L^2\sqrt{\frac{\rho_{\mathrm{P}} A_{\mathrm{P}} + \rho^{\mathrm{i}}_{\mathrm{f}} A_{\mathrm{f}}}{E\sqrt{I^{\mathrm{P}}_{\mathrm{y}} I^{\mathrm{P}}_{\mathrm{z}}}}}$$

$$\mu^* = \frac{\mu}{L^2}\sqrt{\frac{E\sqrt{I^{\mathrm{P}}_{\mathrm{y}} I^{\mathrm{P}}_{\mathrm{z}}}}{\rho_{\mathrm{P}} A_{\mathrm{P}} + \rho^{\mathrm{i}}_{\mathrm{f}} A_{\mathrm{f}}}}\,, \qquad U^* = UL\sqrt{\frac{\rho^{\mathrm{i}}_{\mathrm{f}} A_{\mathrm{f}}}{E\sqrt{I^{\mathrm{P}}_{\mathrm{y}} I^{\mathrm{P}}_{\mathrm{z}}}}}\,, \qquad \beta^{\mathrm{i}}_{\mathrm{f}} = \frac{\rho^{\mathrm{i}}_{\mathrm{f}} A_{\mathrm{f}}}{\rho_{\mathrm{P}} A_{\mathrm{P}} + \rho^{\mathrm{i}}_{\mathrm{f}} A_{\mathrm{f}}}\,, \qquad \beta^{\mathrm{e}}_{\mathrm{f}} = \frac{\pi \rho^{\mathrm{e}}_{\mathrm{f}} D^2_{\mathrm{P}}}{4(\rho_{\mathrm{P}} A_{\mathrm{P}} + \rho^{\mathrm{i}}_{\mathrm{f}} A_{\mathrm{f}})}$$

$$(\Gamma, T^*) = \frac{(P_{\mathrm{i}} A_{\mathrm{f}}, T)L^2}{E\sqrt{I^{\mathrm{P}}_{\mathrm{y}} I^{\mathrm{P}}_{\mathrm{z}}}}\,, \qquad K^*_{\mathrm{stab}} = \frac{K_{\mathrm{stab}} L^3}{E\sqrt{I^{\mathrm{P}}_{\mathrm{y}} I^{\mathrm{P}}_{\mathrm{z}}}}\,, \qquad \gamma = \frac{(\rho_{\mathrm{P}} A_{\mathrm{P}} + \rho^{\mathrm{i}}_{\mathrm{f}} A_{\mathrm{f}}) g L^3}{E\sqrt{I^{\mathrm{P}}_{\mathrm{y}} I^{\mathrm{P}}_{\mathrm{z}}}}\,, \qquad (\delta_{\mathrm{H}}, \delta_{\mathrm{T}}) = (\alpha_{\mathrm{T}}\Delta T, \alpha_{\mathrm{H}}\Delta H)\frac{A_{\mathrm{P}} L^2}{\sqrt{I^{\mathrm{P}}_{\mathrm{y}} I^{\mathrm{P}}_{\mathrm{z}}}}$$

$$\varepsilon = \frac{I^{\mathrm{P}}_{\mathrm{z}}}{I^{\mathrm{P}}_{\mathrm{y}}}\,, \qquad \eta = \frac{\sqrt{I^{\mathrm{P}}_{\mathrm{y}} I^{\mathrm{P}}_{\mathrm{z}}}}{A_{\mathrm{P}} L^2}\,, \qquad \sigma_{\mathrm{A}} = \frac{A_{\mathrm{f}}}{A_{\mathrm{P}}}\,, \qquad (\sigma^{\mathrm{I}}_{\mathrm{y}}, \sigma^{\mathrm{I}}_{\mathrm{z}}) = \left(\frac{I^{\mathrm{y}}_{\mathrm{f}}}{I^{\mathrm{y}}_{\mathrm{P}}}, \frac{I^{\mathrm{z}}_{\mathrm{f}}}{I^{\mathrm{z}}_{\mathrm{P}}}\right), \qquad C^*_{\mathrm{stab}} = \frac{C_{\mathrm{stab}} L^2}{\sqrt{E(\rho_{\mathrm{P}} A_{\mathrm{P}} + \rho^{\mathrm{i}}_{\mathrm{f}} A_{\mathrm{f}})\sqrt{I^{\mathrm{P}}_{\mathrm{y}} I^{\mathrm{P}}_{\mathrm{z}}}}} \tag{30}$$

in which γ is the gravity parameter, Γ is the dimensionless internal pressure, ε is the ratio of lateral area moments, and η is the rotary inertia factor of the system. Also, $\beta^{\mathrm{e}}_{\mathrm{f}}$ and $\beta^{\mathrm{i}}_{\mathrm{f}}$ represent the external and internal flow mass ratios, respectively.

By inserting the dimensionless parameters into the governing equations of the transverse motions of the pipe, using the flow velocity modification factors, and eliminating the asterisk from the dimensionless parameters, the non-dimensional modified equations of the system are obtained as follows by some mathematical manipulation:

$$\begin{aligned}
&\sqrt{\varepsilon}(v'''' + \mu\dot{v}'''') + \big(\Gamma + \delta_{\mathrm{T}} + \delta_{\mathrm{H}} - \gamma(1-x)\big)v'' + \gamma v' + (K_{\mathrm{stab}} v + C_{\mathrm{stab}}\dot{v})\delta_{\mathrm{dir}}(x - x_{\mathrm{stab}}) \\
&\quad + \beta^{\mathrm{e}}_{\mathrm{f}}(\ddot{v} - 2\lambda\Omega\dot{w} - \Omega^2 v) + (\ddot{v} - 2\Omega\dot{w} - \Omega^2 v) + \left(\chi_2 U^2 v'' - 2\chi_1\sqrt{\beta^{\mathrm{i}}_{\mathrm{f}}}U\Omega w' + 2\chi_1\sqrt{\beta^{\mathrm{i}}_{\mathrm{f}}}U\dot{v}'\right) \\
&\quad + (1-\beta^{\mathrm{i}}_{\mathrm{f}})\eta\left(\frac{\Omega^2 v''}{\sqrt{\varepsilon}} - \Omega\left(\sqrt{\varepsilon} + \frac{1}{\sqrt{\varepsilon}}\right)\dot{w}'' - \sqrt{\varepsilon}\ddot{v}''\right) \\
&\quad + \frac{\beta^{\mathrm{i}}_{\mathrm{f}}\eta}{\sigma_{\mathrm{A}}}\left(\frac{\Omega^2\sigma^{\mathrm{y}}_{\mathrm{I}} v''}{\sqrt{\varepsilon}} - \Omega\left(\sigma^{\mathrm{z}}_{\mathrm{I}}\sqrt{\varepsilon} + \frac{\sigma^{\mathrm{y}}_{\mathrm{I}}}{\sqrt{\varepsilon}}\right)\dot{w}'' - \sigma^{\mathrm{z}}_{\mathrm{I}}\sqrt{\varepsilon}\ddot{v}''\right) \\
&\quad - \frac{\eta}{\sigma_{\mathrm{A}}}\left(\chi_4\sigma^{\mathrm{z}}_{\mathrm{I}}\sqrt{\varepsilon}U^2 v'''' + \chi_3\sqrt{\beta^{\mathrm{i}}_{\mathrm{f}}}\Omega U\left(\sigma^{\mathrm{z}}_{\mathrm{I}}\sqrt{\varepsilon} + \frac{\sigma^{\mathrm{y}}_{\mathrm{I}}}{\sqrt{\varepsilon}}\right)w''' + 2\chi_3\sqrt{\beta^{\mathrm{i}}_{\mathrm{f}}}\sigma^{\mathrm{z}}_{\mathrm{I}}\sqrt{\varepsilon}U\dot{v}'''\right) = 0
\end{aligned} \tag{31}$$

$$
\begin{aligned}
&(w'''' + \mu\dot{w}'''')/\sqrt{\varepsilon} + \big(\Gamma + \delta_{\mathrm{T}} + \delta_{\mathrm{H}} - \gamma(1-x)\big)w'' + \gamma w' + (K_{\mathrm{stab}}w + C_{\mathrm{stab}}\dot{w})\delta_{\mathrm{dir}}(x - x_{\mathrm{stab}}) \\
&\quad + \beta_{\mathrm{f}}^{\mathrm{e}}(\ddot{w} + 2\lambda\Omega\dot{v} - \Omega^2 w) + (\ddot{w} + 2\Omega\dot{v} - \Omega^2 w) + \left(\chi_2 U^2 w'' + 2\chi_1\sqrt{\beta_{\mathrm{f}}^{\mathrm{i}}}U\Omega v' + 2\chi_1\sqrt{\beta_{\mathrm{f}}^{\mathrm{i}}}U\dot{w}'\right) \\
&\quad + (1-\beta_{\mathrm{f}}^{\mathrm{i}})\eta\left(\Omega^2\sqrt{\varepsilon}w'' + \Omega\left(\sqrt{\varepsilon} + \frac{1}{\sqrt{\varepsilon}}\right)\dot{w}'' - \frac{\ddot{w}''}{\sqrt{\varepsilon}}\right) \\
&\quad + \frac{\beta_{\mathrm{f}}^{\mathrm{i}}\eta}{\sigma_{\mathrm{A}}}\left(\Omega^2\sigma_{\mathrm{I}}^{\mathrm{z}}\sqrt{\varepsilon}w'' + \Omega\left(\sigma_{\mathrm{I}}^{\mathrm{z}}\sqrt{\varepsilon} + \frac{\sigma_{\mathrm{I}}^{\mathrm{y}}}{\sqrt{\varepsilon}}\right)\dot{v}'' - \frac{\sigma_{\mathrm{I}}^{\mathrm{y}}}{\sqrt{\varepsilon}}\ddot{w}''\right) \\
&\quad - \frac{\eta}{\sigma_{\mathrm{A}}}\left(\chi_4\frac{\sigma_{\mathrm{I}}^{\mathrm{y}}}{\sqrt{\varepsilon}}U^2 w'''' - \chi_3\sqrt{\beta_{\mathrm{f}}^{\mathrm{i}}}\Omega U\left(\sigma_{\mathrm{I}}^{\mathrm{z}}\sqrt{\varepsilon} + \frac{\sigma_{\mathrm{I}}^{\mathrm{y}}}{\sqrt{\varepsilon}}\right)v''' + 2\chi_3\sqrt{\beta_{\mathrm{f}}^{\mathrm{i}}}\frac{\sigma_{\mathrm{I}}^{\mathrm{y}}}{\sqrt{\varepsilon}}U\dot{w}'''\right) = 0
\end{aligned}
\tag{32}
$$

3. Solution methodology

The Laplace transform and the Galerkin discretization scheme are employed for frequency analysis and determination of system stability conditions. The Laplace transform of the temporal derivative can be expressed according to the following relation [51]:

$$
L\big[g^{(\alpha)}(t)\big] = s^{\alpha}G(s) - s^{\alpha-1}g(0) - s^{\alpha-2}g^{(1)}(0) - s^{\alpha-3}g^{(2)}(0) - \cdots - sg^{(\alpha-2)}(0) - g^{(\alpha-1)}(0) \tag{33}
$$

Consequently, by considering the zero initial conditions for the pipe, the dynamic equations of the system in the Laplace domain are rewritten as follows:

$$
\begin{aligned}
&\sqrt{\varepsilon}(v'''' + \mu s v'''') + \big(\Gamma + \delta_{\mathrm{T}} + \delta_{\mathrm{H}} - \gamma(1-x)\big)v'' + \gamma v' + (K_{\mathrm{stab}}v + C_{\mathrm{stab}}sv)\delta_{\mathrm{dir}}(x - x_{\mathrm{stab}}) \\
&\quad + \beta_{\mathrm{f}}^{\mathrm{e}}(s^2 v - 2\lambda\Omega s w - \Omega^2 v) + (s^2 v - 2\Omega s w - \Omega^2 v) \\
&\quad + \left(\chi_2 U^2 v'' - 2\chi_1\sqrt{\beta_{\mathrm{f}}^{\mathrm{i}}}U\Omega w' + 2\chi_1\sqrt{\beta_{\mathrm{f}}^{\mathrm{i}}}U s v'\right) \\
&\quad + (1-\beta_{\mathrm{f}}^{\mathrm{i}})\eta\left(\frac{\Omega^2 v''}{\sqrt{\varepsilon}} - \Omega\left(\sqrt{\varepsilon} + \frac{1}{\sqrt{\varepsilon}}\right)s w'' - \sqrt{\varepsilon}s^2 v''\right) \\
&\quad + \frac{\beta_{\mathrm{f}}^{\mathrm{i}}\eta}{\sigma_{\mathrm{A}}}\left(\frac{\Omega^2\sigma_{\mathrm{I}}^{\mathrm{y}}v''}{\sqrt{\varepsilon}} - \Omega\left(\sigma_{\mathrm{I}}^{\mathrm{z}}\sqrt{\varepsilon} + \frac{\sigma_{\mathrm{I}}^{\mathrm{y}}}{\sqrt{\varepsilon}}\right)s w'' - \sigma_{\mathrm{I}}^{\mathrm{z}}\sqrt{\varepsilon}s^2 v''\right) \\
&\quad - \frac{\eta}{\sigma_{\mathrm{A}}}\left(\chi_4\sigma_{\mathrm{I}}^{\mathrm{z}}\sqrt{\varepsilon}U^2 v'''' + \chi_3\sqrt{\beta_{\mathrm{f}}^{\mathrm{i}}}\Omega U\left(\sigma_{\mathrm{I}}^{\mathrm{z}}\sqrt{\varepsilon} + \frac{\sigma_{\mathrm{I}}^{\mathrm{y}}}{\sqrt{\varepsilon}}\right)w''' + 2\chi_3\sqrt{\beta_{\mathrm{f}}^{\mathrm{i}}}\sigma_{\mathrm{I}}^{\mathrm{z}}\sqrt{\varepsilon}U s v'''\right) = 0
\end{aligned}
\tag{34}
$$

$$
\begin{aligned}
&(w'''' + \mu s w'''')/\sqrt{\varepsilon} + \left(\Gamma + \delta_{\mathrm{T}} + \delta_{\mathrm{H}} - \gamma(1-x)\right)w'' + \gamma w' + (K_{\mathrm{stab}} w + C_{\mathrm{stab}} s w)\delta_{\mathrm{dir}}(x - x_{\mathrm{stab}}) \\
&\quad + \beta_{\mathrm{f}}^{\mathrm{e}}(s^2 w + 2\lambda\Omega s v - \Omega^2 w) + (s^2 w + 2\Omega s v - \Omega^2 w) \\
&\quad + \left(\chi_1 U^2 w'' + 2\chi_2\sqrt{\beta_{\mathrm{f}}^{\mathrm{i}}}U\Omega v' + 2\chi_1\sqrt{\beta_{\mathrm{f}}^{\mathrm{i}}}U s w'\right) \\
&\quad + (1-\beta_{\mathrm{f}}^{\mathrm{i}})\eta\left(\Omega^2\sqrt{\varepsilon}w'' + \Omega\left(\sqrt{\varepsilon} + \frac{1}{\sqrt{\varepsilon}}\right)s w'' - \frac{\ddot{w}''}{\sqrt{\varepsilon}}\right) \\
&\quad + \frac{\beta_{\mathrm{f}}^{\mathrm{i}}\eta}{\sigma_{\mathrm{A}}}\left(\Omega^2\sigma_{\mathrm{I}}^{\mathrm{z}}\sqrt{\varepsilon}w'' + \Omega\left(\sigma_{\mathrm{I}}^{\mathrm{z}}\sqrt{\varepsilon} + \frac{\sigma_{\mathrm{I}}^{\mathrm{y}}}{\sqrt{\varepsilon}}\right)s v'' - \frac{\sigma_{\mathrm{I}}^{\mathrm{y}}}{\sqrt{\varepsilon}}s^2 w''\right) \\
&\quad - \frac{\eta}{\sigma_{\mathrm{A}}}\left(\chi_4\frac{\sigma_{\mathrm{I}}^{\mathrm{y}}}{\sqrt{\varepsilon}}U^2 w'''' - \chi_3\sqrt{\beta_{\mathrm{f}}^{\mathrm{i}}}\Omega U\left(\sigma_{\mathrm{I}}^{\mathrm{z}}\sqrt{\varepsilon} + \frac{\sigma_{\mathrm{I}}^{\mathrm{y}}}{\sqrt{\varepsilon}}\right)v''' + 2\chi_3\sqrt{\beta_{\mathrm{f}}^{\mathrm{i}}}\frac{\sigma_{\mathrm{I}}^{\mathrm{y}}}{\sqrt{\varepsilon}}U s w'''\right) = 0
\end{aligned}
\tag{35}
$$

The above-mentioned dimensionless equations can be discretized via the Galerkin approach. According to this method, the lateral displacements of the pipe are estimated by the following approximated series [52]:

$$v(x,s) = \sum_{j=1}^{\infty} p_j(s)\phi_j(x) \tag{36}$$

$$w(x,s) = \sum_{j=1}^{\infty} q_j(s)\phi_j(x) \tag{37}$$

Here p and q are the generalized coordinates of the system along y- and z- directions, respectively. Also, ϕ is the dimensionless spatial shape function of the system, which is dependent on the boundary conditions and can be specified according to the following relations [53]:

For simply supported boundary conditions:

$$\phi_j(x) = \sin(j\pi x) \tag{38}$$

For cantilevered boundary conditions:

$$\phi_j(x) = \cosh(\lambda_j x) - \cos(\lambda_j x) - \frac{\sinh(\lambda_j) - \sin(\lambda_j)}{\cosh(\lambda_j) + \cos(\lambda_j)}\left(\sinh(\lambda_j x) - \sin(\lambda_j x)\right) \tag{39}$$

The values of λ_{j} in Eq. (39) can be obtained from the characteristic equation $\cosh(\lambda_j)\cos(\lambda_j) = -1$.

For doubly clamped boundary conditions:

$$\phi_j(x) = \cosh(\lambda_j x) - \cos(\lambda_j x) - \frac{\cosh(\lambda_j) - \cos(\lambda_j)}{\sinh(\lambda_j) - \sin(\lambda_j)}\left(\sinh(\lambda_j x) - \sin(\lambda_j x)\right) \tag{40}$$

The values of λ_j in Eq. (40) can be computed from the characteristic equation $\cosh(\lambda_j)\cos(\lambda_j) = 1$.

For clamped-pinned boundary conditions:

$$\phi_j(x) = \cosh(\lambda_j x) - \cos(\lambda_j x) - \frac{\sinh(\lambda_j) - \sin(\lambda_j)}{\cosh(\lambda_j) + \cos(\lambda_j)}\left(\sinh(\lambda_j x) - \sin(\lambda_j x)\right) \tag{41}$$

The values of λ_j in Eq. (41) can be calculated from the characteristic equation $\tanh(\lambda_j) = \tan(\lambda_j)$. In the subsequent section, the number of necessary mode shapes to determine the vibration characteristics of the system is determined.

By designating the appropriate vibration mode shape and inserting the considered approximated series for the lateral displacements into the governing equations and then integrating over the length of the pipe, the dynamic equations of the system can be illustrated in the matrix form as follows:

$$\mathbf{Z}(s) = s^2\begin{bmatrix}\mathbf{M}_1 & \mathbf{0}\\ \mathbf{0} & \mathbf{M}_2\end{bmatrix} + s\begin{bmatrix}\mathbf{G}_1 & \mathbf{G}_2\\ -\mathbf{G}_2 & \mathbf{G}_3\end{bmatrix} + \begin{bmatrix}\mathbf{K}_1 & \mathbf{K}_2\\ -\mathbf{K}_2 & \mathbf{K}_3\end{bmatrix} \tag{42}$$

where $\mathbf{Z}$ is the coefficients matrix and

$$(\mathbf{M}_1)_{sr} = (1+\beta_{\mathrm{f}}^{\mathrm{e}})\int_0^1 \phi_s(x)\phi_r(x)\mathrm{d}x - \left((1-\beta_{\mathrm{f}}^{\mathrm{i}})\sqrt{\varepsilon} + \frac{\beta_{\mathrm{f}}^{\mathrm{i}}\eta\sigma_{\mathrm{I}}^{\mathrm{z}}\sqrt{\varepsilon}}{\sigma_{\mathrm{A}}}\right)\int_0^1 \phi_s(x)\phi_r''(x)\mathrm{d}x \tag{43}$$

$$(\mathbf{M}_2)_{sr} = (1+\beta_{\mathrm{f}}^{\mathrm{e}})\int_0^1 \phi_s(x)\phi_r(x)\mathrm{d}x - \left(\frac{(1-\beta_{\mathrm{f}}^{\mathrm{i}})}{\sqrt{\varepsilon}} + \frac{\beta_{\mathrm{f}}^{\mathrm{i}}\eta\sigma_{\mathrm{I}}^{\mathrm{y}}}{\sigma_{\mathrm{A}}\sqrt{\varepsilon}}\right)\int_0^1 \phi_s(x)\phi_r''(x)\mathrm{d}x \tag{44}$$

$$\begin{aligned}(\mathbf{G}_1)_{sr} = {} & \mu\sqrt{\varepsilon}\int_0^1 \phi_s(x)\phi_r''''(x)\mathrm{d}x + 2\chi_1\sqrt{\beta_{\mathrm{f}}^{\mathrm{i}}}U\int_0^1 \phi_s(x)\phi_r'(x)\mathrm{d}x\\ & - \frac{2\eta\chi_3\sqrt{\beta_{\mathrm{f}}^{\mathrm{i}}}\sigma_{\mathrm{I}}^{\mathrm{z}}\sqrt{\varepsilon}U}{\sigma_{\mathrm{A}}}\int_0^1 \phi_s(x)\phi_r'''(x)\mathrm{d}x + C_{\mathrm{stab}}\phi_s(x_{\mathrm{stab}})\phi_r(x_{\mathrm{stab}})\end{aligned} \tag{45}$$

$$\begin{aligned}(\mathbf{G}_2)_{sr} = {} & -2(\lambda\beta_{\mathrm{f}}^{\mathrm{e}}+1)\Omega\int_0^1 \phi_s(x)\phi_r(x)\mathrm{d}x\\ & - \left((1-\beta_{\mathrm{f}}^{\mathrm{i}})\eta\Omega\left(\sqrt{\varepsilon}+\frac{1}{\sqrt{\varepsilon}}\right) + \frac{\beta_{\mathrm{f}}^{\mathrm{i}}\eta}{\sigma_{\mathrm{A}}}\Omega\left(\sigma_{\mathrm{I}}^{\mathrm{z}}\sqrt{\varepsilon}+\frac{\sigma_{\mathrm{I}}^{\mathrm{y}}}{\sqrt{\varepsilon}}\right)\right)\int_0^1 \phi_s(x)\phi_r''(x)\mathrm{d}x\end{aligned} \tag{46}$$

$$(\mathbf{G}_3)_{sr} = \frac{\mu}{\sqrt{\varepsilon}}\int_0^1 \phi_s(x)\phi_r''''(x)\mathrm{d}x + 2\chi_1\sqrt{\beta_\mathrm{f}^\mathrm{i}}U\int_0^1 \phi_s(x)\phi_r'(x)\mathrm{d}x - \frac{2\eta\chi_3\sqrt{\beta_\mathrm{f}^\mathrm{i}}\sigma_\mathrm{I}^\mathrm{y}U}{\sigma_\mathrm{A}\sqrt{\varepsilon}}\int_0^1 \phi_s(x)\phi_r'''(x)\mathrm{d}x + C_\mathrm{stab}\phi_s(x_\mathrm{stab})\phi_r(x_\mathrm{stab}) \tag{47}$$

$$(\mathbf{K}_1)_{sr} = \left(\sqrt{\varepsilon} - \frac{\eta\chi_4\sigma_\mathrm{I}^\mathrm{z}\sqrt{\varepsilon}U^2}{\sigma_\mathrm{A}}\right)\int_0^1 \phi_s(x)\phi_r''''(x)\mathrm{d}x + \left(\Gamma + \delta_\mathrm{T} + \delta_\mathrm{H} - \gamma(1-x) + \chi_2U^2 + \frac{(1-\beta_\mathrm{f}^\mathrm{i})\eta\Omega^2}{\sqrt{\varepsilon}} + \frac{\beta_\mathrm{f}^\mathrm{i}\eta\Omega^2\sigma_\mathrm{I}^\mathrm{y}}{\sigma_\mathrm{A}\sqrt{\varepsilon}}\right)\int_0^1 \phi_s(x)\phi_r''(x)\mathrm{d}x + \gamma\int_0^1 \phi_s(x)\phi_r'(x)\mathrm{d}x - (1+\beta_\mathrm{f}^\mathrm{e})\Omega^2\int_0^1 \phi_s(x)\phi_r(x)\mathrm{d}x + K_\mathrm{stab}\phi_s(x_\mathrm{stab})\phi_r(x_\mathrm{stab}) \tag{48}$$

$$(\mathbf{K}_2)_{sr} = -2\chi_1\sqrt{\beta_\mathrm{f}^\mathrm{i}}U\Omega\int_0^1 \phi_s(x)\phi_r'(x)\mathrm{d}x - \chi_3\eta\sqrt{\beta_\mathrm{f}^\mathrm{i}}\Omega U\left(\sigma_\mathrm{I}^\mathrm{z}\sqrt{\varepsilon} + \frac{\sigma_\mathrm{I}^\mathrm{y}}{\sqrt{\varepsilon}}\right)\int_0^1 \phi_s(x)\phi_r'''(x)\mathrm{d}x \tag{49}$$

$$(\mathbf{K}_3)_{sr} = \left(\frac{1}{\sqrt{\varepsilon}} - \frac{\eta\chi_4\sigma_\mathrm{I}^\mathrm{y}U^2}{\sigma_\mathrm{A}\sqrt{\varepsilon}}\right)\int_0^1 \phi_s(x)\phi_r''''(x)\mathrm{d}x + \gamma\int_0^1 \phi_s(x)\phi_r'(x)\mathrm{d}x + \left(\Gamma + \delta_\mathrm{T} + \delta_\mathrm{H} - \gamma(1-x) + \chi_2U^2 + (1-\beta_\mathrm{f}^\mathrm{i})\eta\Omega^2\sqrt{\varepsilon} + \frac{\beta_\mathrm{f}^\mathrm{i}\eta\Omega^2\sigma_\mathrm{I}^\mathrm{z}\sqrt{\varepsilon}}{\sigma_\mathrm{A}}\right)\int_0^1 \phi_s(x)\phi_r''(x)\mathrm{d}x - (1+\beta_\mathrm{f}^\mathrm{e})\Omega^2\int_0^1 \phi_s(x)\phi_r(x)\mathrm{d}x + K_\mathrm{stab}\phi_s(x_\mathrm{stab})\phi_r(x_\mathrm{stab}) \tag{50}$$

4. Frequency analysis and stability criteria

Based on the linear algebra theory, the determinant of the coefficients matrix should be equal to zero to determine the non-trivial solution [54].

$$\det[\mathbf{Z}(s)] = 0 \tag{51}$$

The system eigenvalues are the complex-valued roots of the characteristic equation of Eq. (51). The real and imaginary parts of the roots are the modal damping (δ) and vibration frequency (ω) of the system, respectively. It should be noted that static instability (divergence) happens when the real and imaginary components of one of the roots are positive and zero, respectively. Meanwhile, if the real and imaginary components of roots have positive values, dynamic instability (flutter) occurs [55]. By computing the eigenvalues in terms of system parameters, it is possible to determine the effects of key factors on the vibration frequencies and stability of the system.

5. Analytical approach

At the static instability threshold, the lowest vibration frequency of the pipe becomes zero. The pipe loses its effective stiffness for the fundamental vibration mode in this situation. Based on the stability theory of linear gyroscopic structures [36, 56], it has been proven that when the determinant of the stiffness matrix becomes zero, the fundamental vibration frequency of the system also becomes zero. Therefore, to determine the static instability condition of the pipe, one can write for the first vibration mode:

$$(\mathbf{K}_1)_{11}(\mathbf{K}_3)_{11} + (\mathbf{K}_2)_{11}^2 = 0 \quad (52)$$

6. Results and discussion

This section contains comparative studies with experimental and theoretical investigations to verify the presented model and solution approach. Then, the impacts of system parameters, i.e., flow velocity modification factor, viscoelastic coefficient, environmental conditions, geometrical properties, rotary inertia factor, boundary conditions, internal pressure, and stabilizer characteristics, on the vibration behavior and instability thresholds of the system are discovered. In the following, the dimensionless results are discussed to generalize the research outcomes better.

6.1. Comparative studies

In this subsection, firstly, a convergence examination is performed. Afterward, several comparative studies for pipes conveying fluid with symmetric cross-sections (i.e., Figures (2-5)) and spinning structures with asymmetric cross-sections (i.e., Figure 6) are presented. Before comparison studies, a convergence test is conducted to choose the suitable number of shape functions for the calculation of the vibration frequencies of the system. The accuracy of the acquired results of the Galerkin discretization technique is greatly dependent on the appropriate number of shape functions. Table 1 indicates the convergence study for the two lowest backward and forward vibration frequencies. As shown, when the number of shape functions increases, all the vibration frequencies of the system converge to a specific value. It can be observed that when eight vibration modes are considered, the converged vibration frequencies can be acquired.

Hence, eight basis functions are sufficient to obtain reasonable outcomes for further computations in the current study.

Table 1. Convergence study of dimensionless vibration frequencies of the system with internal circular cross-section when ε=1, U=1, Ω=5, β_f^i=0.2^2, η=γ=T=μ=Γ=0

Number of vibration modes	ω_1^b	ω_1^f	ω_2^b	ω_2^f
N=2	4.35253	14.35253	33.99069	43.99069
N=4	**4.35250**	**14.35250**	33.97925	43.97925
N=6	**4.35250**	**14.35250**	33.97906	43.97906
N=8	**4.35250**	**14.35250**	**33.97904**	**43.97904**
N=10	**4.35250**	**14.35250**	**33.97904**	**43.97904**

The bold numbers are suitable approximations for the dimensionless vibration frequencies of the system.

In Figure 2, the critical flow velocities of a simply supported pipe under an axial tensile force are displayed. The corresponding flow velocities to divergence and flutter instabilities are known as divergence flow velocity (U_d) and flutter flow velocity (U_f), respectively. According to the figure, as the axial tensile force enhances, the divergence and flutter flow velocities improve. In addition, as is clear, the results of the present study are in good agreement with the theoretical and experimental results presented by Jiang et al. [57]. It should be mentioned that eight vibration modes are considered in the Galerkin discretization scheme to calculate the system eigenvalues.

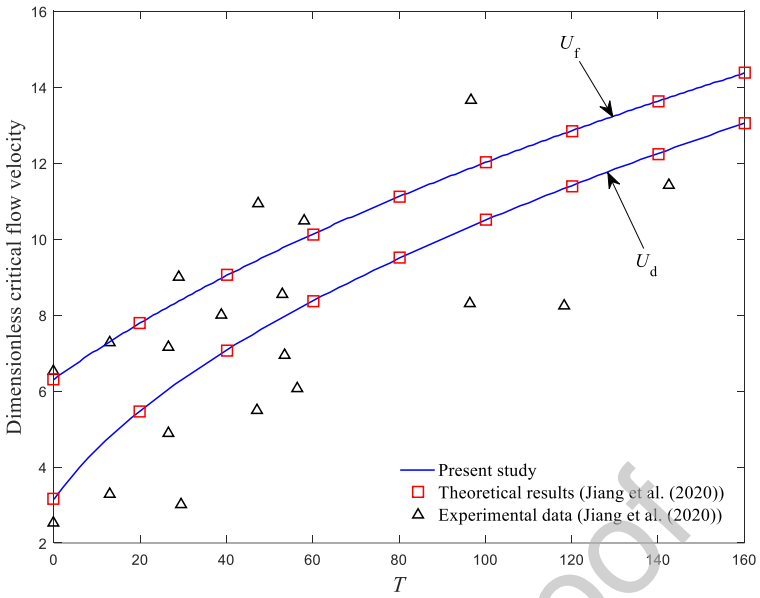

Fig. 2. Dimensionless critical flow velocities of a simply supported pipe against the dimensionless axial tension force without the effects of stabilizer, external fluid, and environmental loads when $\Omega=\eta=\gamma=\mu=\Gamma=0$

In Figure 3, the stability map of an upward cantilevered pipe ($\gamma<0$) in the γ-U plane is drawn and compared with the published theoretical and experimental results. According to this diagram, the stable/flutter region of the pipe shrinks/expands by reducing the gravity parameter. Also, at small values of the gravity parameter, the system undergoes divergence instability. In addition, as can be observed, the results of the present investigation are consistent with the experimental and numerical data reported by Paidoussis [58].

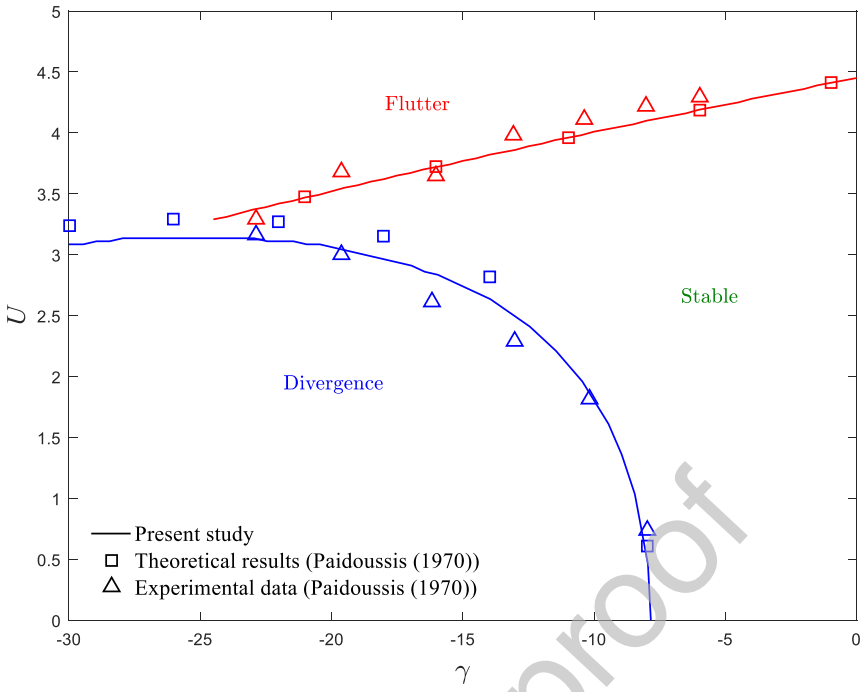

Fig. 3. Stability map of a cantilevered pipe in the γ-U plane without the effects of stabilizer, external fluid, and environmental loads when $\Omega=\eta=T=\mu=\Gamma=0$

In Figures 4 (a, b), the Campbell diagram and modal damping versus the spin speed are presented for a spinning simply supported beam surrounded by an annular fluid medium, respectively. In this figure, the first two vibration frequencies of the system are plotted against the spin speed. According to this figure, the backward (lower branch) and forward (upper branch) frequency decreases and increases, respectively, by sweeping the spin speed. When the first vibration frequency of the pipe becomes zero, the system undergoes divergence instability, and the corresponding spin speed is called the divergence spin speed (Ω_d). Also, when the backward and forward frequency branches coalesce, the system experiences flutter instability, and the corresponding spin speed is called the flutter spin speed (Ω_f). As can be seen, the numerical results of the present research are compared with the analytical results presented by Abdollahi et al. [47], and a close agreement is observed.

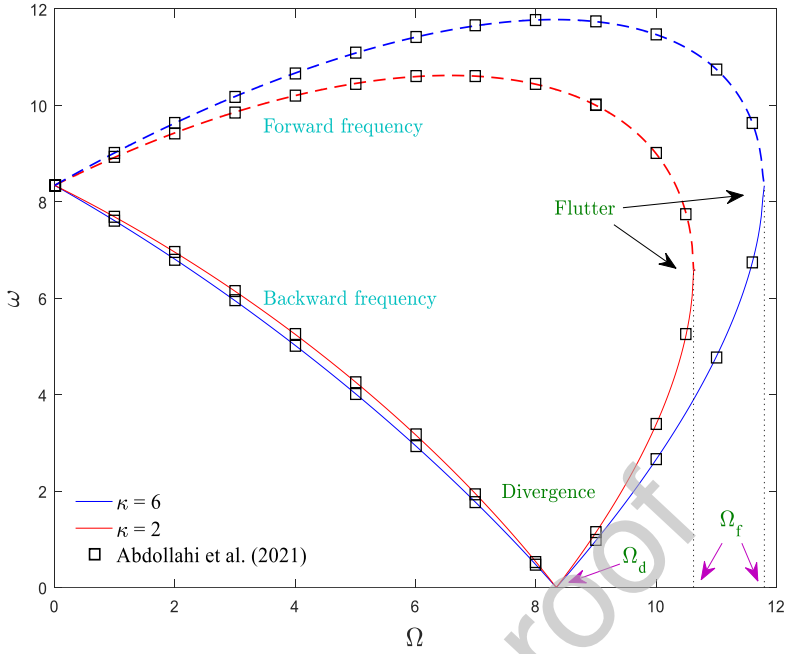

(a)

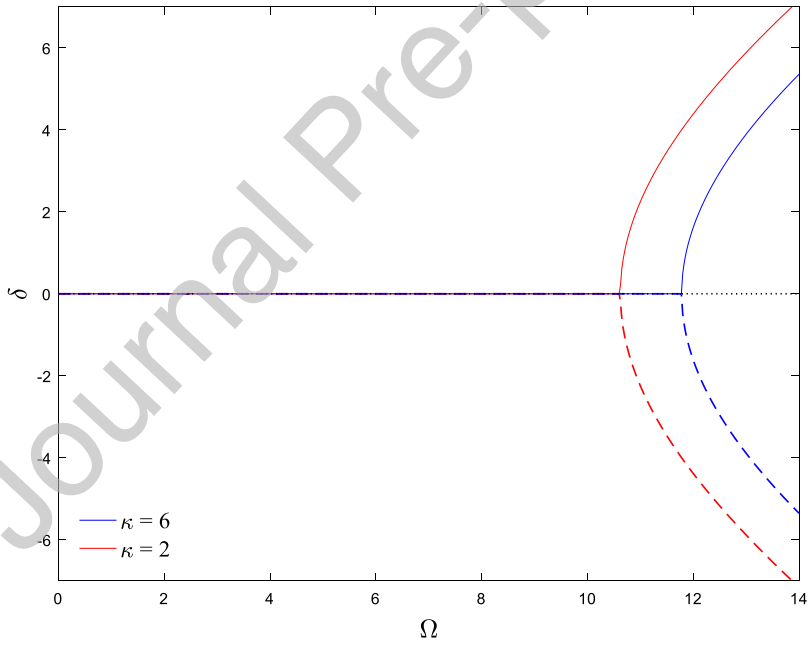

(b)

Fig. 4. (a) Dimensionless vibration frequencies and (b) modal damping of a simply supported beam immersed in an annular fluid medium against the dimensionless spin speed without the effects of stabilizer and environmental loads when ε=1, β_f^e=0.4, U=η=γ=T=μ=Γ=0

In Figure 5 (a, b), the first four vibration frequencies and modal damping of a spinning simply supported pipe are depicted in terms of the flow velocity. According to the diagram, the backward and forward frequencies descend as the flow velocity ascends. When the fundamental backward frequency of the system becomes zero, the pipe undergoes static instability. The forward and backward frequency branches merge by further ascending the flow velocity, and the pipe experiences dynamic instability. It should be mentioned that a similar pattern can also be observed for higher vibration modes. Also, as is apparent, the current research outcomes demonstrate an excellent correlation with those obtained by Liang et al. [59].

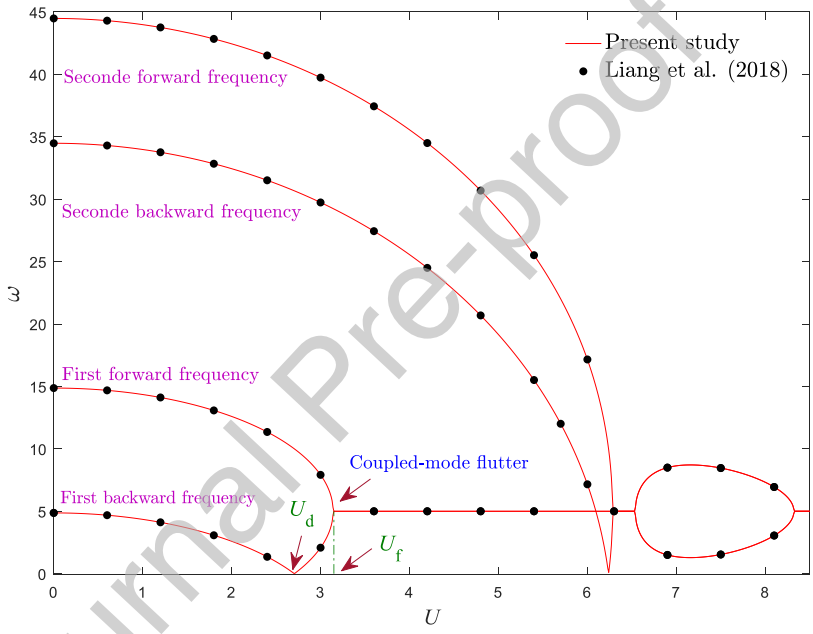

(a)

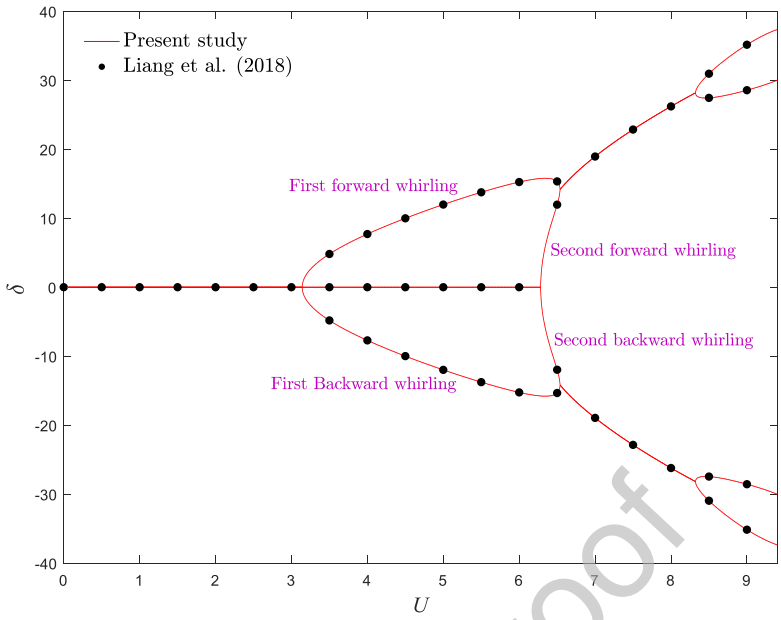

(b)

Fig. 5. (a) Dimensionless vibration frequencies and (b) modal damping of a spinning simply supported pipe against the dimensionless flow velocity without the effects of stabilizer, external fluid, and environmental loads when ε=1, Ω=5, β_f^i=0.2^2, η=γ=T=μ=Γ=0

In Figures 6 (a, b), the first four vibration frequencies and modal damping of a spinning cantilevered beam with an asymmetric (rectangular) cross-section are shown versus the spin speed, respectively. Based on the figure, the instability in the system has a static nature (divergence), and the maximum difference between the instability margins of the present method and those attained by the dynamic stiffness method in [60] is 1.4 %.

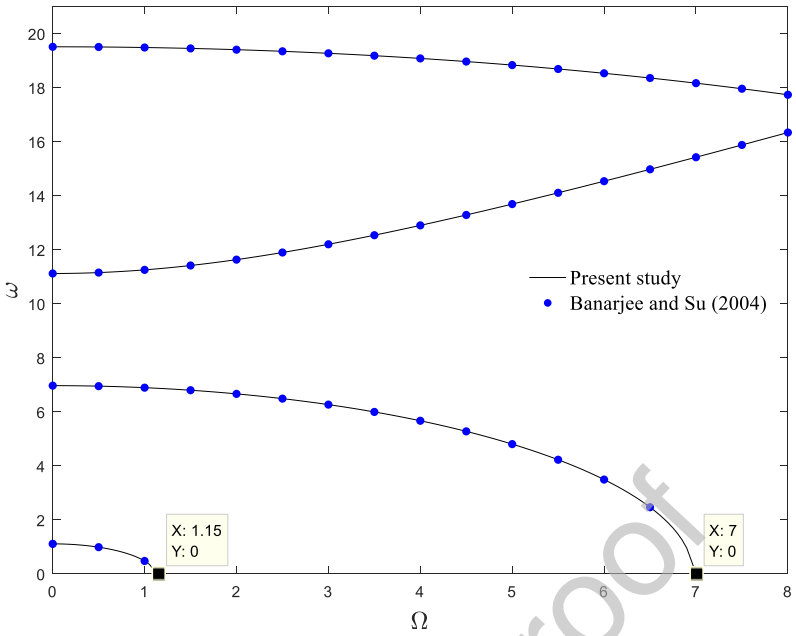

(a)

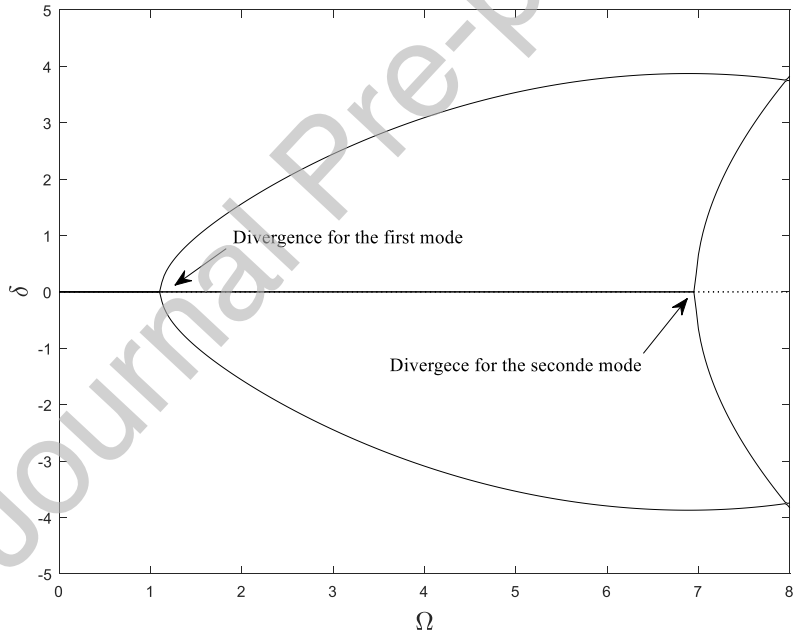

(b)

Fig. 6. (a) Dimensionless vibration frequencies and (b) modal damping of a cantilevered beam with rectangular cross-section against the dimensionless spin speed and without the effects of stabilizer, external fluid, and environmental loads when ε=0.01, U=η=γ=T=μ=Γ=0

6.2. Parametric studies

In the following, to determine the influence of critical parameters on the structural stability and vibration behavior, the geometric and material properties of the system are considered according to Table 2 unless otherwise mentioned.

Table 2: Geometry and material properties of the system [13, 41, 61]

Property	Value
EI	8.9782 Nm^2
D_P	0.05 m
$a=b$	0.02 m
ρ_P	2766 kg/m^3
L	2 m
ρ_f	1000 kg/m^3
α_H	0.44 $(wt\%H_2O)^{-1}$
α_T	11×10^{-6} K^{-1}

Figure 7 shows the importance of the flow velocity modification factor in the dynamic behavior of a cantilevered pipe. In this figure, the first three vibration frequencies of the system are plotted versus the flow velocity. It can be affirmed that when the effect of the flow velocity modification factor is ignored, the system first becomes unstable by increasing the flow velocity at U=10.75. Then, the pipe regains stability by further increasing the flow velocity at U=11.62. Finally, at U=12.62, it becomes unstable again and retains instability for higher flow velocities. This remarkable dynamic feature, known as the sequence of instability-restabilization-instability transitions, occurs for non-conservative systems conveying flow [33]. As can be observed, by considering the flow velocity modification effect, contrary to the first mode, the vibration frequencies of higher modes increase with the increment of the flow velocity. Also, as is evident, the effect of the flow velocity modification on the frequency branches of the system becomes more evident by ascending the flow velocity. It is visible that the higher vibration modes are more sensitive to the non-uniformity of the flow velocity profile. Besides, by considering the flow velocity modification effect, the system experiences the flutter phenomenon at a lower flow velocity (i.e., U=8.1). Based on this diagram, the system experiences the mode-exchange phenomenon (intersection of frequency branches), a unique characteristic of cantilevered flow-

conveying pipes [58]. It is worth stating that, unlike non-conservative cantilevered pipes, supported pipes experience instability conditions via the divergence and couple-mode flutter phenomena (see Figure 5).

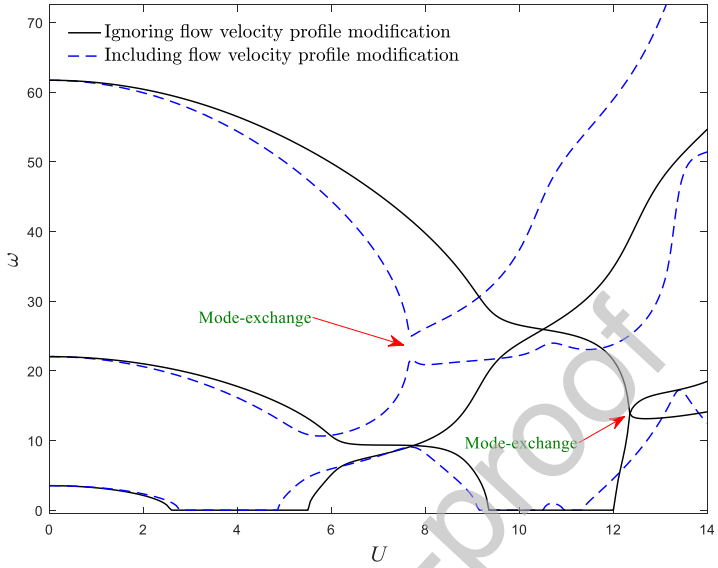

(a)

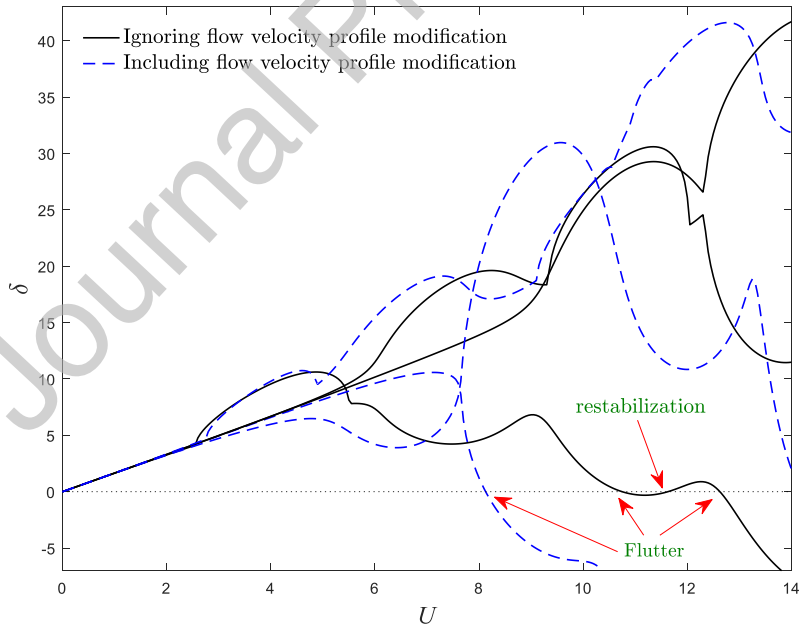

(b)

Fig. 7. (a) Dimensionless vibration frequencies and (b) modal damping of a cantilevered pipe against the dimensionless flow velocity without the effects of stabilizer, external fluid, and environmental

loads when β_f^i=0.68, Ω=γ=η=T=μ=Γ=0

In Figure 8, the stability map of a cantilevered pipe is portrayed in the γ-U plane, and the necessity of considering the flow velocity profile modification is revealed. According to this figure, flutter instability happens in the system under the operating conditions inside the depicted region. The instability boundaries consist of the s-shaped segments associated with the instability-restabilization-instability sequence [33]. It is seen that the higher the gravity parameter, the wider the stable operational region becomes. This point can be justified by the fact that the gravity parameter has a stiffening effect on the pipe. Also, it is observable that when the flow velocity modification effect is considered for the dynamic equations of the pipe, the stability of the system is reduced, especially for higher values of the gravity parameter. Furthermore, the s-shaped segments of the flutter boundaries are shifted toward higher gravity parameters by considering the flow velocity modification effect, and the restabilization phenomenon occurs in a wider range of gravity parameters. According to the dynamic equations of the system, considering a non-uniform velocity distribution for the internal flow has considerable impacts on the Coriolis and centrifugal forces. In general, the Coriolis force weakens and the centrifugal force magnifies by considering the flow velocity modification effect. Since Coriolis and centrifugal forces induce stabilizing and destabilizing effects on the pipe, one can infer that the flow velocity modification effect leads to stability degradation in the pipe. Based on Figures 7 and 8, it can be concluded that the consideration of the flow velocity modification effect is of great importance for the accurate characterization of dynamic behavior and vibration stability of flow-carrying systems.

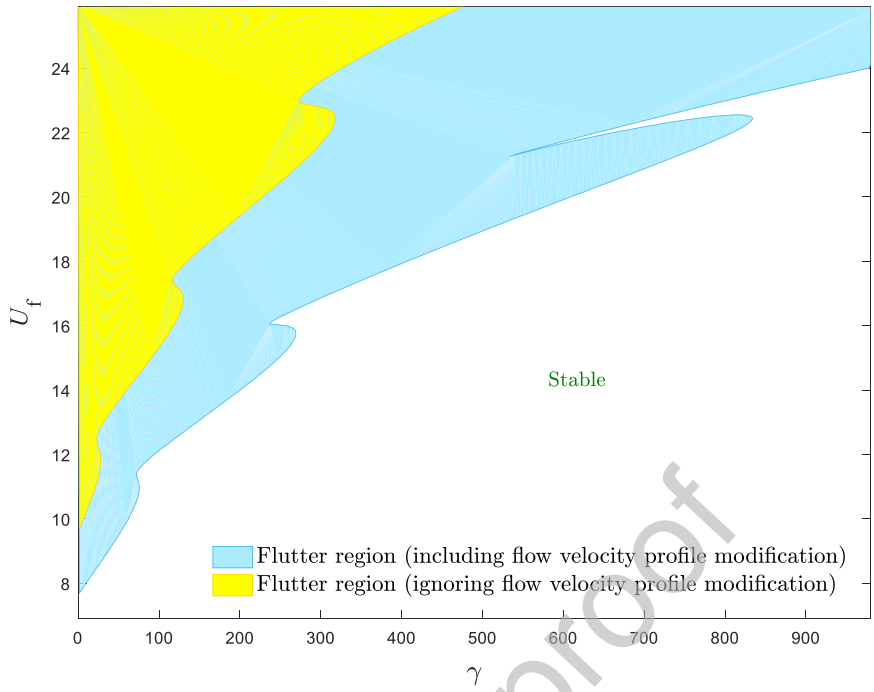

Fig. 8. Dimensionless flutter flow velocity of a cantilevered pipe versus the gravity parameter without the effects of stabilizer, external fluid, and environmental loads when β_f^i=0.55, Ω=η=T=μ=Γ=0

Figure 9 presents the Campbell diagram for a doubly clamped beam with an asymmetric cross-section submerged in a fluid-filled annular medium. According to the figure, when the system has a symmetric cross-section, the divergence instability occurs only at a specific spin speed. Also, forward and backward vibration frequencies have the same value at Ω=0 for the system with a symmetric cross-section. While the system with an asymmetric cross-section experiences static instability for a range of spin speeds. It should be noted that as the ratio of the lateral area moments approaches the unity value, the divergence spin speed range becomes narrower. Also, when the lateral area moments of the system are unequal, the forward and backward vibration frequencies have different values at Ω=0. In addition, it is observed that when the system is surrounded by an external annular fluid medium, after the divergence instability occurrence, the system becomes stable again. As the spin speed enhances further, the forward vibration frequency decreases, and at higher spin speeds, the system loses its stability again via the coupled-mode flutter bifurcation. As is obvious, compared with the system with an asymmetric cross-section, the system with a symmetric cross-section has a higher/lower backward/forward vibration frequency and a smaller flutter spin speed.

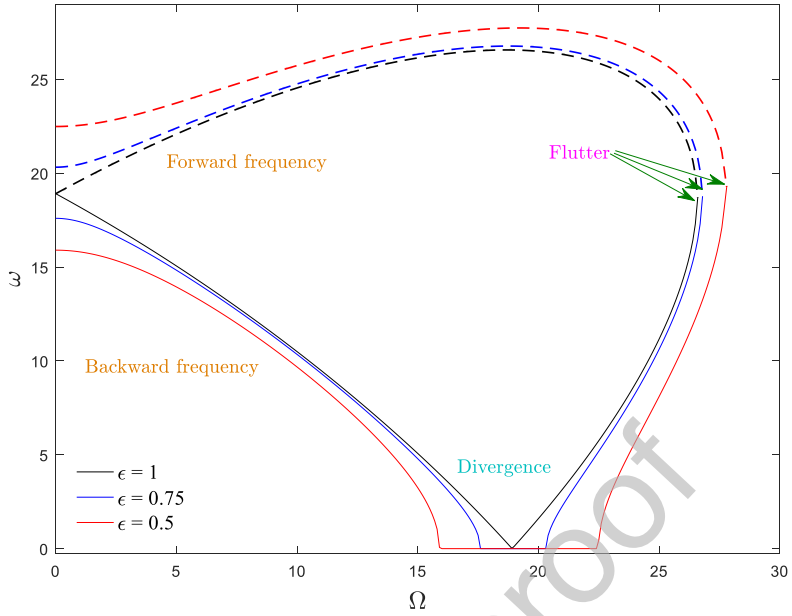

Fig. 9. Campbell diagram of a doubly clamped beam without the effects of stabilizer and environmental loads when κ=5, β_f^e=0.4, Ω=U=η=T=μ=Γ=0

In Figure 10, the effect of rotary inertia on the Campbell diagram of a pipe containing flow with both ends clamped is examined. Based on this figure, when the rotary inertia effects are not considered for the system, the variations of the vibration frequencies are linear with the spin speed variations. So, in the pre-buckling state, by increasing the spin speed, the backward/forward frequency of the system decreases/increases linearly, respectively. Also, in the post-buckling state, frequency branches become parallel and exhibit an increasing trend with ascending spin speed. While by considering the rotary inertia effects, frequency branches are not parallel in the post-buckling state and display a nonlinear pattern with spin speed variations. In addition, when the rotary inertia effects are considered negligible, the frequency branches intersect at infinity, and flutter instability is not observed in the stability evolution of the system. While if the rotary inertia parameter has a non-zero value, the system experiences the flutter phenomenon. Additionally, enhancing the rotary inertia parameter diminishes the divergence and flutter spin speeds. In simple words, the system is more prone to instability for high rotary inertia parameters. To better comprehend the rotary inertia effect on the dynamic behavior of spinning pipes, the vibration frequencies and modal damping of a cantilevered pipe conveying flow in

terms of the spin speed are plotted in Figures 11 (a, b), respectively. It can be seen that the non-conservative pipes conveying flow lose their stability via a Hopf bifurcation (i.e., a single-mode flutter). By comparing Figures 10 and 11, it can be understood that for supported systems in the post-buckling state, by considering rotary inertia effects, the backward/forward frequency branch is above/below the case without rotary inertia effects. Whereas this trend is reversed for the cantilevered system.

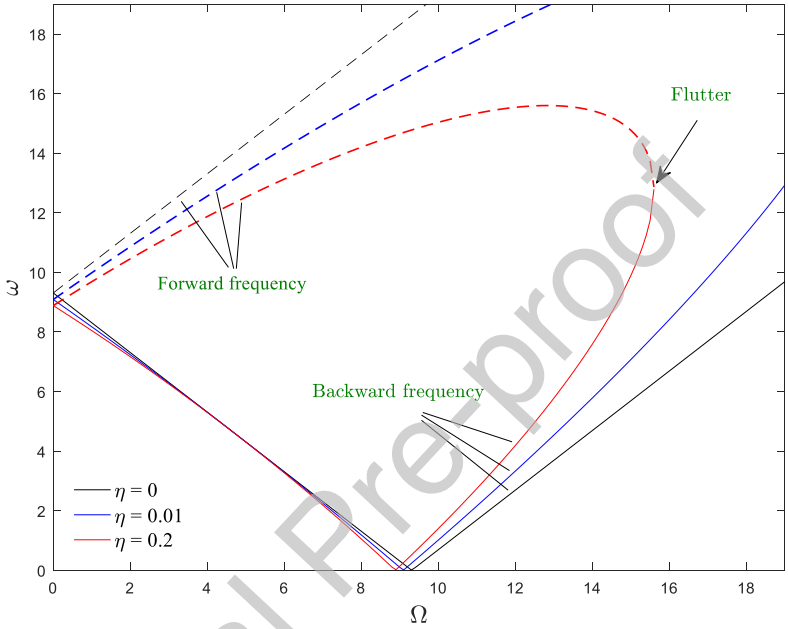

Fig. 10. Campbell diagram of a simply supported pipe without the effects of stabilizer, external fluid, and environmental loads when U=1, γ=T=μ=Γ=0

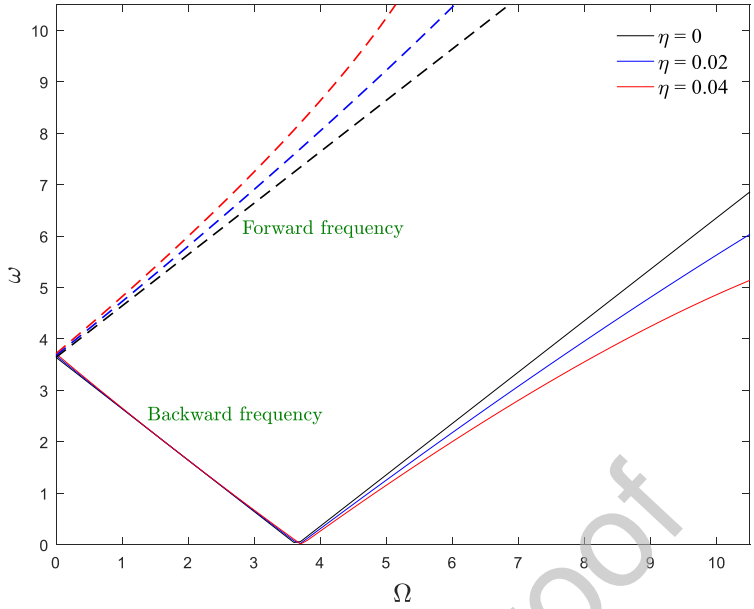

(a)

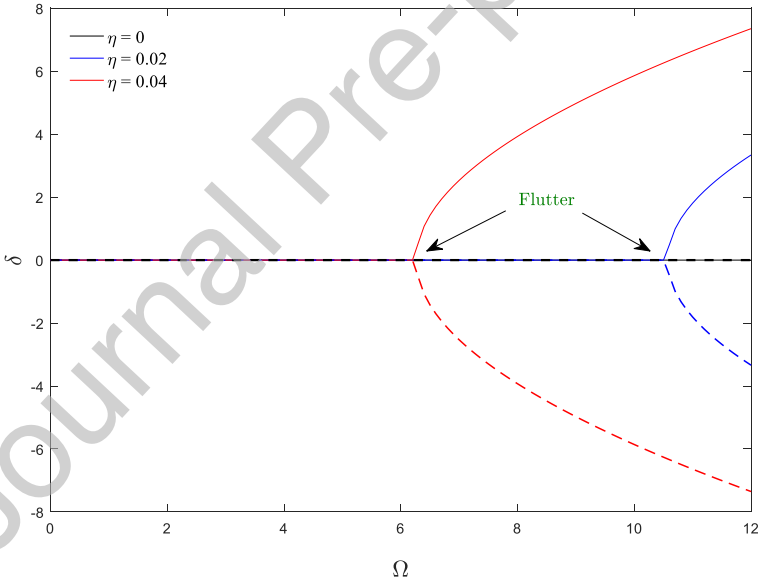

(b)

Fig. 11. (a) Dimensionless vibration frequency and (b) modal damping of the cantilevered pipe against the dimensionless spin speed without the effects of stabilizer, external fluid, and environmental loads when U=1, γ=T=μ=Γ=0

Figure 12 depicts the effect of hygro-thermal environments on the Campbell diagram of a clamped-pinned flow-conveying pipe. Based on this figure, when the system operates in moist

and thermal fields, its vibration frequencies decline. Also, the inclusion of moisture and thermal effects leads to the decrement of divergence and flutter spin speeds and induces destabilizing effects on the system. Indeed, thermal loads generate compressive stresses in supported systems. Also, in wet environments, degradation conditions occur in the system by absorbing water molecules. This physically implies that the system operation in hygro-thermal fields leads to stiffness-reduction effects and the shrinkage of the stability region. As illustrative data indicated in Figures (9-12), it can be deduced that the doubly clamped system has a higher vibration frequency and better stability among the supported boundary conditions.

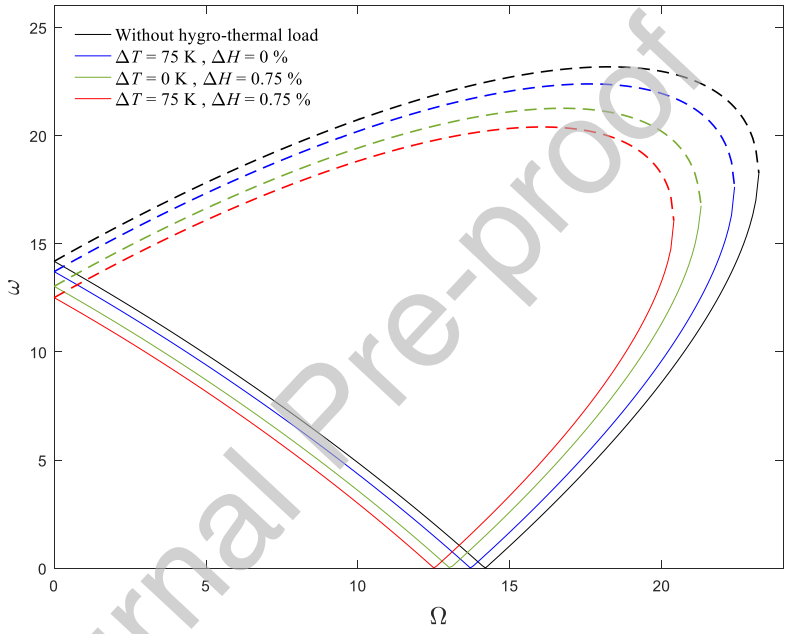

Fig. 12. Campbell diagram of a clamped-pinned pipe without the effects of stabilizer and external fluid when U=1, β_f^i=0.5, η=0.02, γ=T=μ=Γ=0

Figure 13 shows the dependency of the vibration behavior of a spinning simply supported pipe carrying flow on the viscoelastic coefficient. According to this figure, for the viscoelastically damped system, the divergence flow velocity does not change, but the system experiences a flutter condition instantly after the divergence state. Hence, one can infer that as the viscosity coefficient increases, the flutter flow velocity of the system decreases. In addition, by considering the pipe's viscoelastic property, the modal damping values are non-zero at U=0. Also, the modal damping curves lose their symmetry to the abscissa. In addition, the

phenomenon of coupling between frequency branches is not observed by considering the viscoelastic properties of the pipe.

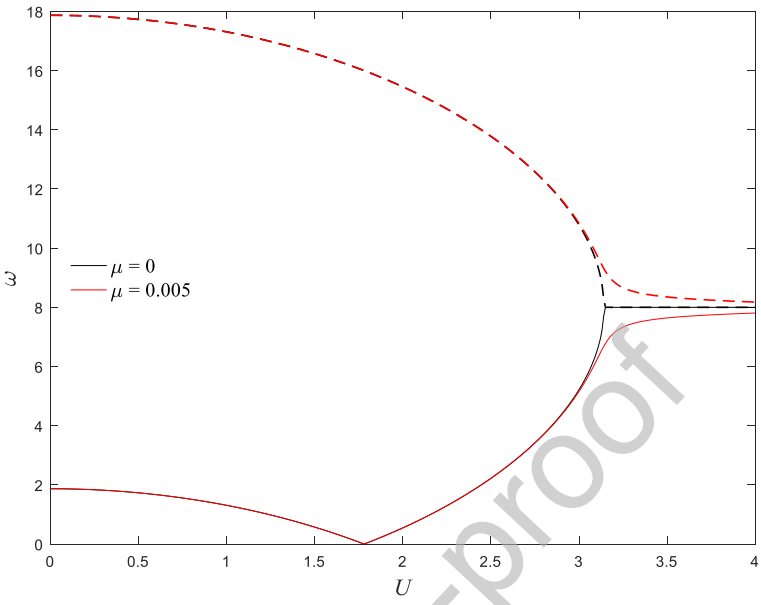

(a)

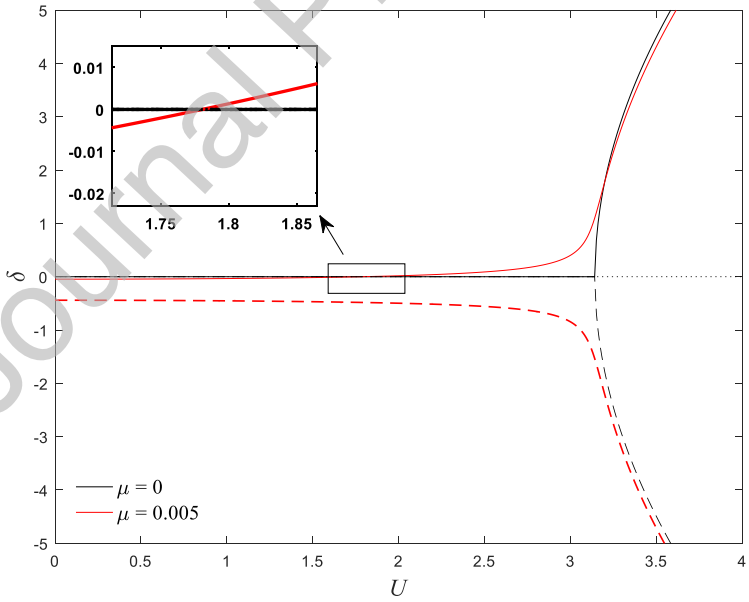

(b)

Fig. 13. (a) Dimensionless vibration frequency and (b) modal damping of a spinning simply supported pipe against the dimensionless flow velocity without the effects of stabilizer, external fluid, and

environmental loads when Ω=8, β_f^i=0.5, γ=T=Γ=0

In Figure 14, the stability map of a simply supported pipe conveying flow is drawn in the Γ-Ω plane. It is well-known that the equivalent stiffness of the system descends by ascending the pressure inside the pipe. Thus, when the rotary inertia effects are ignored in the system, it can be observed that at low spin speeds, by ascending the internal pressure, the pipe first experiences divergence instability at a certain spin speed. By continuing the increment of the internal pressure, the pipe becomes stable again, and at high internal pressure values, it undergoes flutter instability and becomes no longer stable. At high spin speeds, the pipe does not experience static instability by increasing the internal pressure, and at high internal pressure values, it only undergoes dynamic instability. Also, the system only experiences divergence instability at low internal pressure values by increasing the spin speed. While at high internal pressure values, it undergoes flutter instability for all spin speeds. In other words, when the internal pressure increases to such an extent that the divergence spin speed becomes zero, divergence instability is not observed in the stability evolution. When the rotary inertia effect is considered in the model, the instability region of the system expands, and the corresponding divergence spin speed also decreases. This destabilizing effect can be attributed to the mass addition effects of the rotary inertia parameter. It should be noted that at low internal pressure values, the pipe experiences both static and dynamic instability by considering the rotary inertia effect (see Figures 10 and 11). Another noticeable point in this stability map is that the divergence instability only occurs on the depicted borders, and the divergence region does not exist in the stability map of the spinning pipe with an internal circular cross-section.

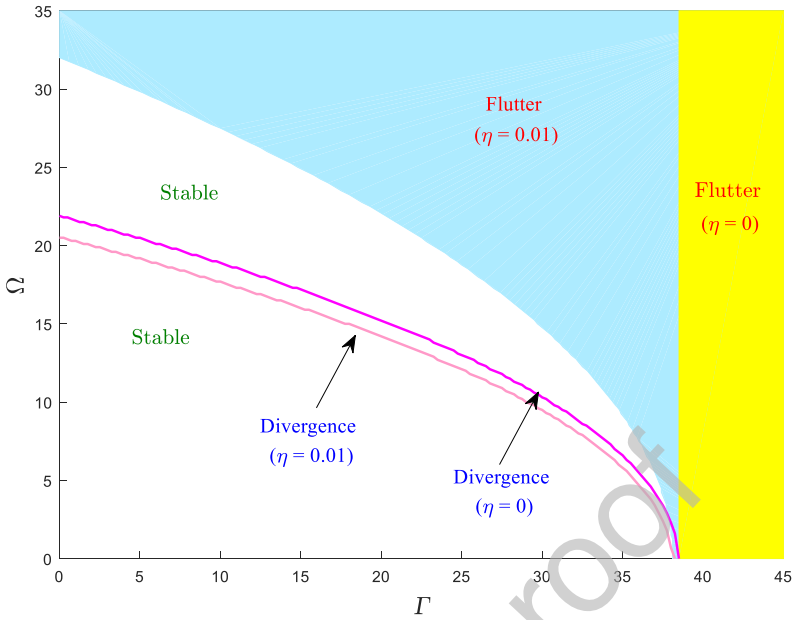

Fig. 14. Stability map of a simply supported pipe in the Γ-Ω plane without the effects of stabilizer, external fluid, and environmental loads when U=1, β_f^i=0.5, γ=T=μ=Γ=0

Figure 15 demonstrates the stability map of a spinning simply supported pipe with an internal elliptical cross-section in the Γ-U plane. It should be mentioned that since the ratio of the lateral area moments of the system is not equal to unity, the divergence instability region exists in the stability map. In the case of an asymmetric cross-section, for low flow velocity or spin speed values, the stability evolution of the system is "stable - divergence - stable - flutter". The system does not have an initial stable region for medium flow velocity or spin speed values. Also, for high flow velocity or spin speed values, the system undergoes flutter instability after initial stable working conditions. In addition, for very high values of flow velocity or spin speed, the system only experiences flutter instability conditions.

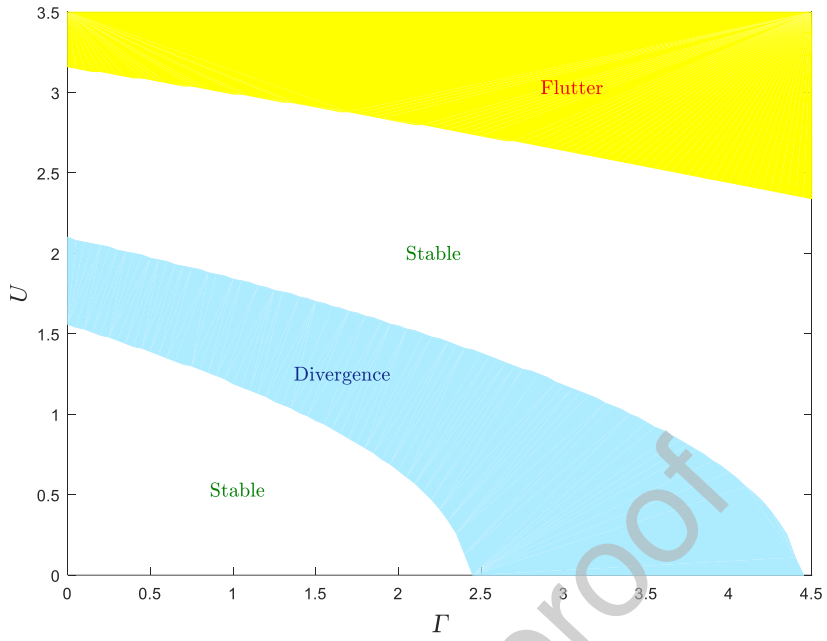

Fig. 15. Stability map of a spinning simply supported pipe in the Γ-U plane without the effects of stabilizer, external fluid, and environmental loads when Ω=8, β_f^i=0.5, b=2a=0.02, η=γ=T=μ=Γ=0

In Figure 16, the effect of the rotary inertia parameter on the stability of simply supported flow-conveying pipes submerged in an external fluid medium in the Ω-β_f^e plane is displayed. Because the considered system has a symmetric (circular) internal cross-section, in this case, the divergence instability border is observed in the stability map. As can be seen, the divergence spin speed and flutter instability threshold decrease by ascending the external mass ratio. This stability reduction feature originates from the added mass of the external fluid. Also, the critical spin speeds are reduced by considering the rotary inertia effects, and this decrement effect is more tangible for low values of the external mass ratio.

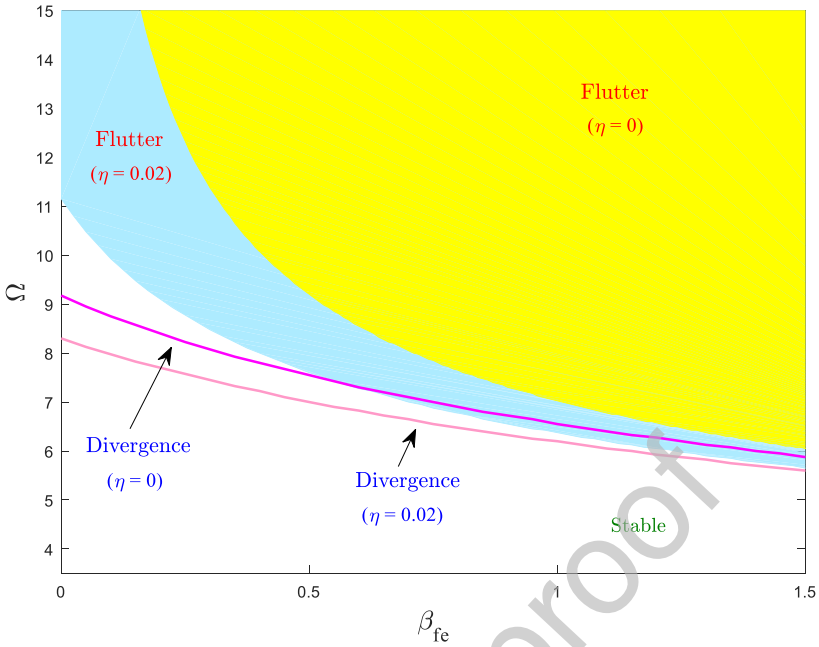

Fig. 16. Stability map of a simply supported pipe in the Γ-Ω plane without the effects of stabilizer and environmental loads when U=1, β_f^i=0.5, κ=2, γ=T=μ=Γ=0

Figure 17 depicts the stable and unstable regions of a spinning simply supported pipe with an internal elliptical cross-section in the κ-U plane. Note that the existence of the divergence instability region in the stability map can be attributed to the asymmetric (elliptical) cross-section of the pipe. It is visible that the unstable flutter region enlarges by decreasing the external to internal diameter ratio. It is notable that the variation of the external to internal diameter ratio has a greater influence on the flutter instability threshold of the system for small values of κ. While the impact of the external to internal diameter ratio variation is less prominent on the flutter boundary for large values of κ. However, the boundaries of the divergence instability region do not depend on the external to internal diameter ratio variation. Figures 16 and 17 indicate that if the pipe operates in a narrower external fluid domain with a denser fluid, it has less stability.

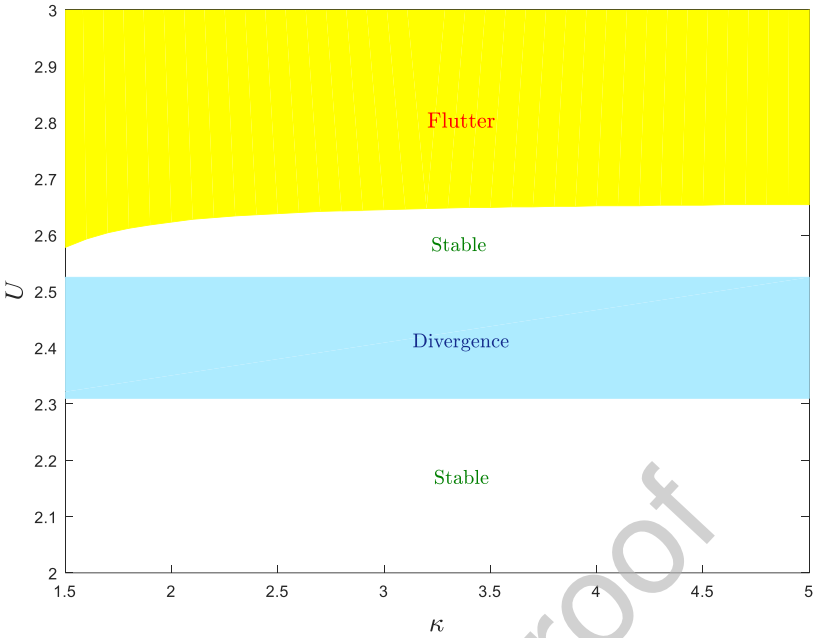

Fig. 17. Stability map of a simply supported pipe in the Γ-Ω plane without the effects of stabilizer and environmental loads when Ω=5, β_f^i=0.5, β_f^e=0.2, b=2a=0.02, η=γ=T=μ=Γ=0

Figures 18 (a, b) indicate the critical spin speeds of the simply supported fluid-conveying pipe in terms of the aspect ratio (e=a/b) of the system cross-section. In Figure 18(a), by neglecting the rotary inertia effects, the system only undergoes divergence instability by increasing the spin speed. As observed, when the internal cross-section is circular (i.e., a/b=1), it experiences static instability only at a specific spin speed. While for the system with an internal elliptical cross-section (i.e., $a\neq b$), divergence instability occurs over a range of spin speeds. So, the higher or lower the aspect ratio value than unity, the wider the divergence region. Figure 18 (b) shows that the divergence instability zone displaces toward lower spin speeds by considering the rotary inertia effects. Also, at high spin speeds, the pipe undergoes flutter instability. Notably, the flutter instability region expands by an increase in the aspect ratio. Generally, ascending the rotary inertia parameter tends to weaken the stability of the system.

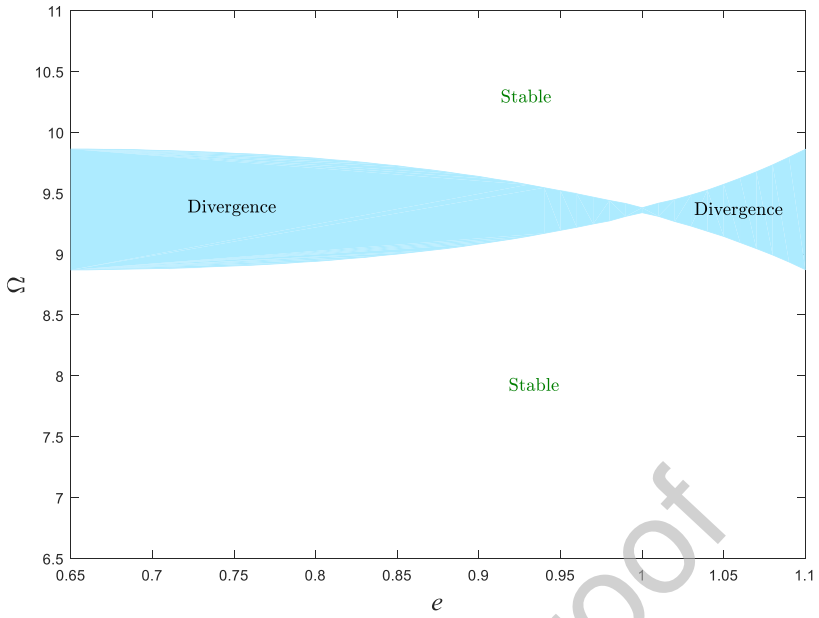

(a)

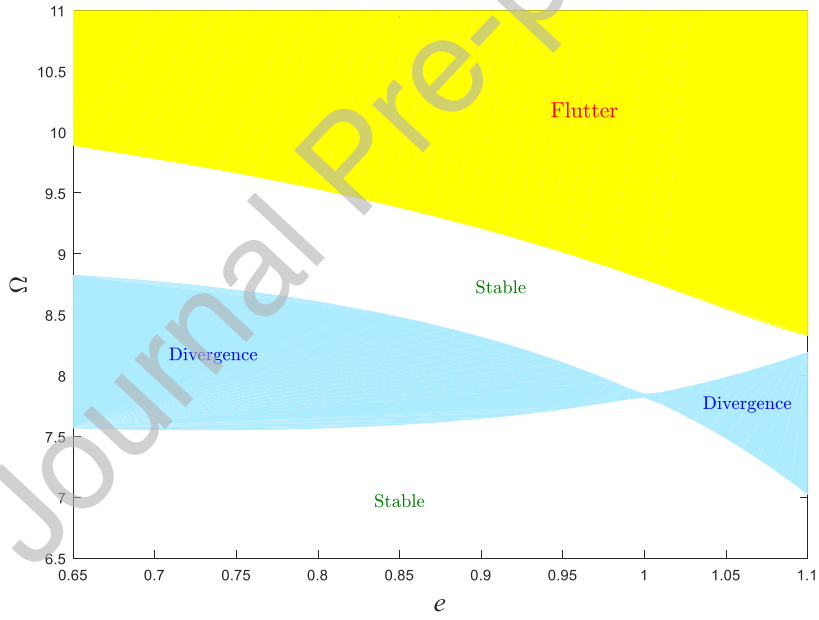

(b)

Fig. 18. Stability map of a simply supported pipe in the e-**Ω** plane without the effects of stabilizer, external fluid, and environmental loads when U=1, β_f^i=0.5, b=0.02, γ=T=Γ=0 (a) η=0 (b) η=0.035

The stabilizer is an essential component in the drilling tool assembly. To understand the stabilizer effects on the vibration behavior and stability of the system, Figures 19 and 20 are

presented for conservative and non-conservative systems, respectively. In Figure 19, the Campbell diagram is drawn for the clamped-pinned pipe with an internal elliptical cross-section attached to the stabilizer with different installation positions. As shown, by approaching the stabilizer installation position to the pipe middle, the system has higher critical spin speeds and is more stable. In addition, the system stability is improved by increasing the stabilizer stiffness. Generally, the attachment of a stiffer stabilizer to the mid-span of a supported pipe improves the system stability.

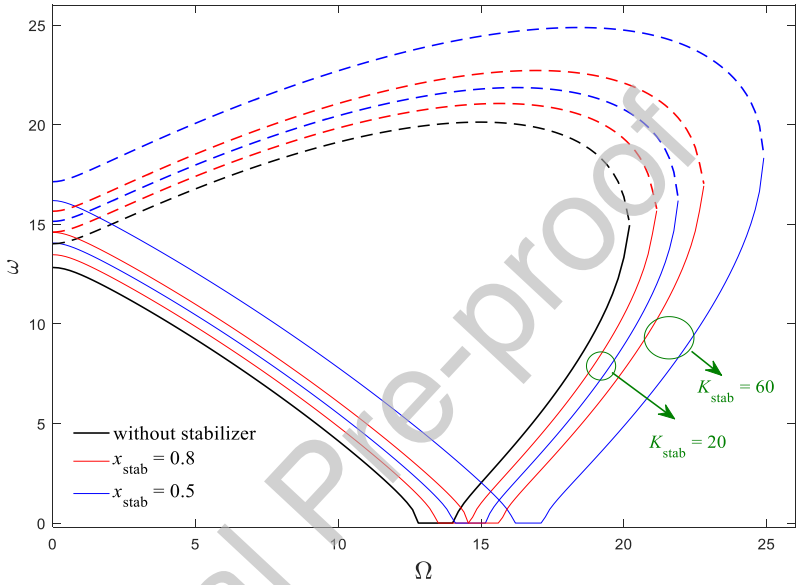

Fig. 19. Campbell diagram of a clamped-pinned pipe without the environmental effects when U=1, β_f^i=0.5, β_f^i=0.2, κ=6, a=η=0.01, γ=T=μ=Γ=c_{stab}=0

In Figure 20 (a, b), the stability maps of the spinning and non-spinning cantilevered pipes are shown in the K_{stab}-U plane, respectively, when the stabilizer is installed at the free end. According to Figure 20 (a), by increasing the stabilizer stiffness, the non-spinning system experiences both static and dynamic instabilities. It should be noted that divergence instability happens for high stabilizer stiffness values. Also, the divergence instability boundaries do not depend on the stabilizer damping value. It can be observed that the flutter instability occurs for all stabilizer stiffness values by ascending the flow velocity. Besides, the flutter flow velocity increases/decreases by increasing the stabilizer stiffness/damping. As shown in Figure 20 (b), the divergence instability region is not observed in the stability map of the spinning system. Also, the flutter instability region of the system expands by increasing the stabilizer damping. Also, by

increasing the stabilizing damping and enlarging the flutter instability zone, a detached stable region is formed in the stability map of the system. The lower boundary of this detached stable region is related to the restabilization threshold [62].

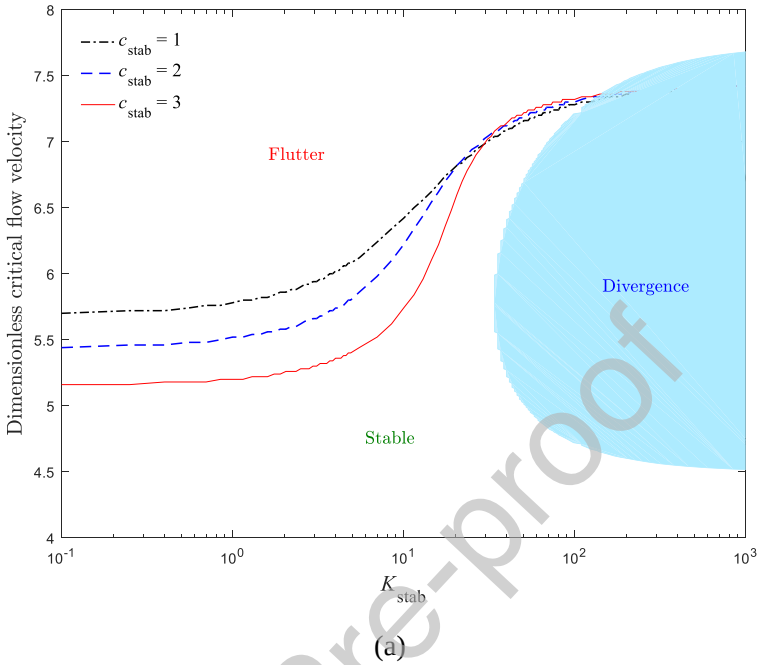

(a)

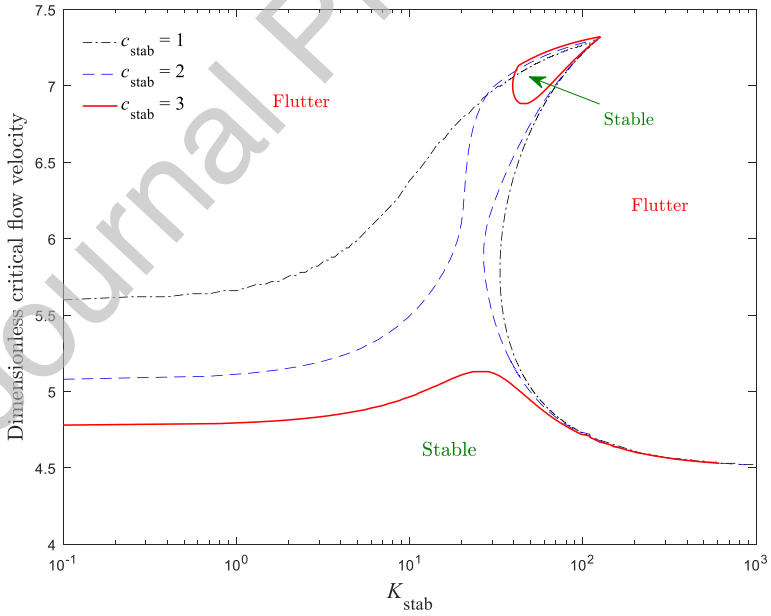

(b)

Fig. 20. Stability map of a cantilevered pipe in the K_{stab}-U plane without the effects of external fluid and environmental loads when β_f^i=0.2, γ=T=Γ=0 (a) Ω=0 (b) Ω=5

In Figure 21, the divergence borders of the submerged pipe are depicted in the U-Ω plane. It can be seen that by ascending the internal flow velocity and spin speed, the static instability threshold of the system decreases. According to the figure, when the structure is subjected to a compressive/tensile force, the divergence threshold of the pipe decreases/increases. Also, the system stability is reduced by considering the mass-addition and stiffness-softening effects of the rotary inertia factor. Another important feature in this figure is the consistency of the deduced results from numerical and analytical approaches. It should be noted that the analytical method presented by Abdollahi and his colleagues [47] is suitable only when the external fluid is considered (i.e., the internal flow effects are neglected). The analytical approach of the current research is even applicable when internal flow effects are also taken into account.

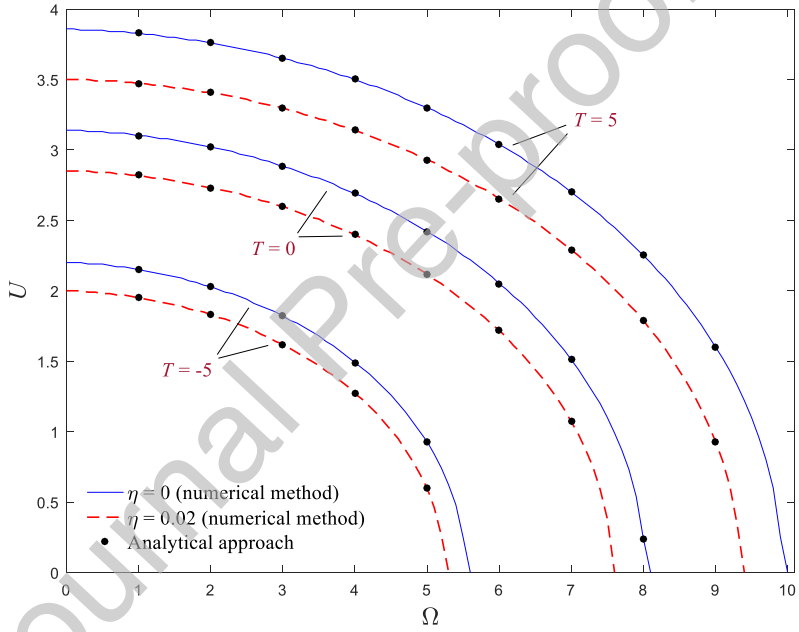

Fig. 21. Divergence borders of a submerged simply supported pipe in the U-Ω plane without the effects of stabilizer and environmental loads when β_f^i=0.5, β_f^e=0.4, κ=2, γ=μ=Γ=0

7. Conclusions

In this article, an in-depth investigation to identify the stability and dynamics of spinning viscoelastic flow-conveying pipes with an internal elliptical cross-section immersed in an external fluid annular medium is conducted. To derive the governing dynamic equations, the flow velocity modification factor for the Coriolis force, centrifugal load, and gyroscopic effects

are taken into account. Also, the rotary inertia effects, hygro-thermal loads, and the internal pressure of the pipe are considered. The vibration frequencies and stability margins are determined. In addition, the static instability threshold of the pipe is computed using an analytical approach. Finally, the effects of the influential factors, such as stabilizer characteristics, boundary conditions, external fluid mass ratio, and geometric properties, on the vibration characteristics and unstable situations of the system are clarified. The main findings of the current research can be summarized as follows:

- ✓ The vibration frequencies and stability of the cantilevered system are reduced by considering the flow velocity modification factor.
- ✓ The greater the gravity parameter, the higher the system stability.
- ✓ In the presence of hygro-thermal conditions, a lower spin speed leads to instability.
- ✓ By considering the rotary inertia effects, the flutter instability is observed in the Campbell diagram, and the system stability is weakened.
- ✓ In the stability evaluation of the viscoelastically damped system, the couple-mode flutter bifurcation does not occur.
- ✓ The flutter instability zone expands by increasing the external fluid mass ratio and external to internal diameter ratio. Also, the external to internal diameter ratio does not affect the static instability boundary.
- ✓ In the stability map of the system with dissimilar transverse area moments, a static instability region is observed instead of a divergence instability border.
- ✓ When the spinning pipe is submerged in an external fluid, the divergence instability region condenses by approaching the aspect ratio value to unity. Also, by considering the rotary inertia effects, the flutter spin speed is reduced with an increase in the aspect ratio.
- ✓ For conservative systems, the system stability is improved by increasing the stabilizer stiffness and approaching the installation location to the pipe middle. For non-conservative systems, the system stability decreases with an increase in the stabilizer damping value.

Acknowledgment

The Iran National Science Foundation (INSF) is acknowledged for the postdoctoral fellowship granted to Dr. Ali Ebrahimi-Mamaghani (INSF-Grant No. 97009741).

References

[1] Y. Zhang, T. Liu, and W. Zhang, "Nonlinear resonant responses, mode interactions, and multitime periodic and chaotic oscillations of a cantilevered pipe conveying pulsating fluid under external harmonic force," *Complexity*, vol. 2020, pp. 1-26, 2020.

[2] Y. Xia, M. Shi, C. Zhang, C. Wang, X. Sang, R. Liu, *et al.*, "Analysis of flexural failure mechanism of ultraviolet cured-in-place-pipe materials for buried pipelines rehabilitation based on curing temperature monitoring," *Engineering Failure Analysis*, vol. 142, p. 106763, 2022.

[3] A. Ebrahimi-Mamaghani, N. Mostoufi, R. Sotudeh-Gharebagh, and R. Zarghami, "Vibrational analysis of pipes based on the drift-flux two-phase flow model," *Ocean Engineering*, vol. 249, p. 110917, 2022.

[4] A. Ebrahimi-Mamaghani, R. Sotudeh-Gharebagh, R. Zarghami, and N. Mostoufi, "Thermo-mechanical stability of axially graded Rayleigh pipes," *Mechanics Based Design of Structures and Machines*, vol. 50, pp. 412-441, 2022.

[5] T. E. Elaikh, N. M. Abed, and A. Ebrahimi-Mamaghani, "Free vibration and flutter stability of interconnected double graded micro pipes system conveying fluid," in *IOP Conference Series: Materials Science and Engineering*, 2020, p. 022128.

[6] Y. Zhang, M. Yao, W. Zhang, and B. Wen, "Dynamical modeling and multi-pulse chaotic dynamics of cantilevered pipe conveying pulsating fluid in parametric resonance," *Aerospace Science and Technology*, vol. 68, pp. 441-453, 2017.

[7] C. Yang, J. Zhang, and Z. Huang, "Numerical study on cavitation–vortex–noise correlation mechanism and dynamic mode decomposition of a hydrofoil," *Physics of Fluids*, vol. 34, p. 125105, 2022.

[8] M. P. Païdoussis, "Pipes conveying fluid: A fertile dynamics problem," *Journal of Fluids and Structures*, vol. 114, p. 103664, 2022.

[9] M. Paıdoussis and G. Li, "Pipes conveying fluid: a model dynamical problem," *Journal of fluids and Structures*, vol. 7, pp. 137-204, 1993.

[10] A. Ebrahimi-Mamaghani, R. Sotudeh-Gharebagh, R. Zarghami, and N. Mostoufi, "Dynamics of two-phase flow in vertical pipes," *Journal of Fluids and Structures*, vol. 87, pp. 150-173, 2019.

[11] H. Sarparast, A. Alibeigloo, S. S. Kesari, and S. Esfahani, "Size-dependent dynamical analysis of spinning nanotubes conveying magnetic nanoflow considering surface and environmental effects," *Applied Mathematical Modelling*, 2022.

[12] X. Pan, W. Wu, X. Yu, L. Lu, C. Guo, and Y. Zhao, "Typical electrical, mechanical, electromechanical characteristics of copper-encapsulated REBCO tapes after processing in temperature under 250℃," *Superconductor Science and Technology*, 2023.

[13] Q. Qian, L. Wang, and Q. Ni, "Instability of simply supported pipes conveying fluid under thermal loads," *Mechanics Research Communications*, vol. 36, pp. 413-417, 2009.

[14] R. S. Reddy, S. Panda, and A. Gupta, "Nonlinear dynamics of an inclined FG pipe conveying pulsatile hot fluid," *International Journal of Non-Linear Mechanics*, vol. 118, p. 103276, 2020.

[15] I. C. Esfahani and H. Sun, "A droplet-based micropillar-enhanced acoustic wave (μPAW) device for viscosity measurement," *Sensors and Actuators A: Physical*, vol. 350, p. 114121, 2023.

[16] S. Ji, R. Ran, I. Chiniforooshan Esfahani, K.-t. Wan, and H. Sun, "A New Microfluidic Device Integrated with Quartz Crystal Microbalance to Measure Colloidal Particle Adhesion," in *ASME International Mechanical Engineering Congress and Exposition*, 2021, p. V005T05A075.

[17] A. E. Ebrahimi-Mamaghani, S. Khadem, and S. Bab, "Vibration control of a pipe conveying fluid under external periodic excitation using a nonlinear energy sink," *Nonlinear Dynamics*, vol. 86, pp. 1761-1795, 2016.

[18] A. E. Ebrahimi-Mamaghani, S. E. Khadem, S. Bab, and S. M. Pourkiaee, "Irreversible passive energy transfer of an immersed beam subjected to a sinusoidal flow via local nonlinear attachment," *International Journal of Mechanical Sciences*, vol. 138, pp. 427-447, 2018.

[19] Q. Ni, Y. Luo, M. Li, and H. Yan, "Natural frequency and stability analysis of a pipe conveying fluid with axially moving supports immersed in fluid," *Journal of Sound and Vibration*, vol. 403, pp. 173-189, 2017.
[20] Q. Huang, T. Lin, and M. Safarpour, "Flow-induced vibration attenuation of a viscoelastic pipe conveying fluid under sinusoidal flow using a nonlinear absorber," *Mechanics Based Design of Structures and Machines*, vol. 50, pp. 1673-1703, 2022.
[21] M. Heshmati, "Influence of an eccentricity imperfection on the stability and vibration behavior of fluid-conveying functionally graded pipes," *Ocean Engineering*, vol. 203, p. 107192, 2020.
[22] L. Wang, H. Liu, Q. Ni, and Y. Wu, "Flexural vibrations of microscale pipes conveying fluid by considering the size effects of micro-flow and micro-structure," *International Journal of Engineering Science*, vol. 71, pp. 92-101, 2013.
[23] M. Heshmati, F. Daneshmand, and Y. Amini, "Vibration and stability analysis of functionally graded elliptical pipes conveying fluid with flow velocity profile modification," *Engineering with Computers*, pp. 1-16, 2021.
[24] Z.-X. Zhou and O. Koochakianfard, "Dynamics of spinning functionally graded Rayleigh tubes subjected to axial and follower forces in varying environmental conditions," *The European Physical Journal Plus*, vol. 137, pp. 1-35, 2022.
[25] F. Liang, A. Gao, X.-F. Li, and W.-D. Zhu, "Nonlinear parametric vibration of spinning pipes conveying fluid with varying spinning speed and flow velocity," *Applied Mathematical Modelling*, vol. 95, pp. 320-338, 2021.
[26] R. Bahaadini and A. R. Saidi, "Stability analysis of thin-walled spinning reinforced pipes conveying fluid in thermal environment," *European Journal of Mechanics-A/Solids*, vol. 72, pp. 298-309, 2018.
[27] F. Liang, X.-D. Yang, W. Zhang, and Y.-J. Qian, "Dynamical modeling and free vibration analysis of spinning pipes conveying fluid with axial deployment," *Journal of Sound and Vibration*, vol. 417, pp. 65-79, 2018.
[28] M. Eftekhari and M. Hosseini, "On the stability of spinning functionally graded cantilevered pipes subjected to fluid-thermomechanical loading," *International Journal of Structural Stability and Dynamics*, vol. 16, p. 1550062, 2016.
[29] F. Liang, X.-D. Yang, W. Zhang, and Y.-J. Qian, "Vibrations in 3D space of a spinning supported pipe exposed to internal and external annular flows," *Journal of Fluids and Structures*, vol. 87, pp. 247-262, 2019.
[30] K. Zhu and J. Chung, "Vibration and stability analysis of a simply-supported Rayleigh beam with spinning and axial motions," *Applied Mathematical Modelling*, vol. 66, pp. 362-382, 2019.
[31] M. Khoshroo and M. Eftekhari, "Probabilistic analysis of drill string under uncertain conditions for flow velocity and axial compressive load," *Applied Ocean Research*, vol. 122, p. 103142, 2022.
[32] M. A. Aouadi and F. Lakrad, "On mathematical modelling of linear flexural vibrations of spinning Rayleigh beams," *Journal of Sound and Vibration*, vol. 430, pp. 17-35, 2018.
[33] M. P. Paidoussis, *Fluid-structure interactions: slender structures and axial flow* vol. 1: Academic press, 1998.
[34] F. Liang, A. Gao, and X.-D. Yang, "Dynamical analysis of spinning functionally graded pipes conveying fluid with multiple spans," *Applied Mathematical Modelling*, vol. 83, pp. 454-469, 2020.
[35] X. Wang and X. Lyu, "Experimental study on vertical water entry of twin spheres side-by-side," *Ocean Engineering*, vol. 221, p. 108508, 2021.
[36] A. Ebrahimi-Mamaghani, A. Forooghi, H. Sarparast, A. Alibeigloo, and M. Friswell, "Vibration of viscoelastic axially graded beams with simultaneous axial and spinning motions under an axial load," *Applied Mathematical Modelling*, vol. 90, pp. 131-150, 2021.
[37] K. Zhang, Z. Wang, G. Chen, L. Zhang, Y. Yang, C. Yao, *et al.*, "Training effective deep reinforcement learning agents for real-time life-cycle production optimization," *Journal of Petroleum Science and Engineering*, vol. 208, p. 109766, 2022.
[38] M. Shahgholi and S. A. Ghasabi, "Nonlinear dynamic behavior and bifurcation analysis of a rotating viscoelastic size-dependent beam based on non-classical theories," *The European Physical Journal Plus*, vol. 135, pp. 1-25, 2020.

[39] Q. Fu, M. Gu, J. Yuan, and Y. Lin, "Experimental study on vibration velocity of piled raft supported embankment and foundation for ballastless high-speed railway," *Buildings*, vol. 12, p. 1982, 2022.
[40] S. Bab, S. E. Khadem, A. Abbasi, and M. Shahgholi, "Dynamic stability and nonlinear vibration analysis of a rotor system with flexible/rigid blades," *Mechanism and Machine Theory*, vol. 105, pp. 633-653, 2016.
[41] M. R. Barati, N. M. Faleh, and A. M. Zenkour, "Dynamic response of nanobeams subjected to moving nanoparticles and hygro-thermal environments based on nonlocal strain gradient theory," *Mechanics of Advanced Materials and Structures*, vol. 26, pp. 1661-1669, 2019.
[42] X. Chang, X. Li, L. Yang, and Y. Li, "Vibration characteristics of the stepped drill string subjected to gas-structure interaction and spinning motion," *Journal of Sound and Vibration*, vol. 450, pp. 251-275, 2019.
[43] P. F. Pai, X. Qian, and X. Du, "Modeling and dynamic characteristics of spinning Rayleigh beams," *International Journal of Mechanical Sciences*, vol. 68, pp. 291-303, 2013.
[44] S. Sahebkar, M. Ghazavi, S. Khadem, and M. Ghayesh, "Nonlinear vibration analysis of an axially moving drillstring system with time dependent axial load and axial velocity in inclined well," *Mechanism and Machine Theory*, vol. 46, pp. 743-760, 2011.
[45] Z. Li, K. Wang, W. Li, S. Yan, F. Chen, and S. Peng, "Analysis of surface pressure pulsation characteristics of centrifugal pump magnetic liquid sealing film," *Internal flow mechanism of modern hydraulic machinery*, vol. 16648714, p. 124, 2023.
[46] R. Ye, P. Liu, K. Shi, and B. Yan, "State damping control: A novel simple method of rotor UAV with high performance," *IEEE access*, vol. 8, pp. 214346-214357, 2020.
[47] R. Abdollahi, R. D. Firouz-abadi, and M. Rahmanian, "On the stability of rotating pipes conveying fluid in annular liquid medium," *Journal of Sound and Vibration*, vol. 494, p. 115891, 2021.
[48] S. Esfahani, S. E. Khadem, and A. E. Mamaghani, "Nonlinear vibration analysis of an electrostatic functionally graded nano-resonator with surface effects based on nonlocal strain gradient theory," *International Journal of Mechanical Sciences*, vol. 151, pp. 508-522, 2019.
[49] V. Borjalilou and M. Asghari, "Mathematical modeling of anisotropic hyperelastic cylindrical thick shells by incorporating thickness deformation and compressibility with application to arterial walls," *International Journal of Structural Stability and Dynamics*, 2022.
[50] C. Guo, C. Zhang, and M. Paidoussis, "Modification of equation of motion of fluid-conveying pipe for laminar and turbulent flow profiles," in *Seismic Safety Evaluation of Concrete Dams*, ed: Elsevier, 2013, pp. 221-237.
[51] C. Liu, Y. Zhao, Y. Wang, T. Zhang, and H. Jia, "Hybrid dynamic modeling and analysis of high-speed thin-rimmed gears," *Journal of Mechanical Design*, vol. 143, 2021.
[52] S. Chucheepsakul, N. Srinil, and P. Petchpeart, "A variational approach for three-dimensional model of extensible marine cables with specified top tension," *Applied Mathematical Modelling*, vol. 27, pp. 781-803, 2003.
[53] A. Ebrahimi-Mamaghani, H. Sarparast, and M. Rezaei, "On the vibrations of axially graded Rayleigh beams under a moving load," *Applied Mathematical Modelling*, vol. 84, pp. 554-570, 2020.
[54] Q. Zhu, J. Chen, and G. Gou, "Ameliorated Longitudinal Critically Refracted 390 Attenuation Velocity Method for Welding Residual Stress Measurement," *Journal of*, vol. 391, pp. 267-275.
[55] J. Song, A. Mingotti, J. Zhang, L. Peretto, and H. Wen, "Accurate Damping Factor and Frequency Estimation for Damped Real-Valued Sinusoidal Signals," *IEEE Transactions on Instrumentation and Measurement*, vol. 71, pp. 1-4, 2022.
[56] L. Lu, W. Wu, Y. Gao, C. Pan, X. Yu, C. Zhang, *et al.*, "Study on current discrepancy and redistribution of HTS non-insulation closed-loop coils during charging/discharging and subsequent transient process toward steady-state operation," *Superconductor Science and Technology*, vol. 35, p. 095001, 2022.
[57] T. Jiang, H. Dai, and L. Wang, "Three-dimensional dynamics of fluid-conveying pipe simultaneously subjected to external axial flow," *Ocean Engineering*, vol. 217, p. 107970, 2020.
[58] M. Paidoussis, "Dynamics of tubular cantilevers conveying fluid," *Journal of Mechanical Engineering Science*, vol. 12, pp. 85-103, 1970.

[59] F. Liang, X.-D. Yang, Y.-J. Qian, and W. Zhang, "Transverse free vibration and stability analysis of spinning pipes conveying fluid," *International Journal of Mechanical Sciences*, vol. 137, pp. 195-204, 2018.
[60] J. Banerjee and H. Su, "Dynamic stiffness formulation and free vibration analysis of a spinning composite beam," *Computers & structures*, vol. 84, pp. 1208-1214, 2006.
[61] Y. Huo and Z. Wang, "Dynamic analysis of a vertically deploying/retracting cantilevered pipe conveying fluid," *Journal of Sound and Vibration*, vol. 360, pp. 224-238, 2016.
[62] H. Dai, L. Wang, and Q. Ni, "Dynamics of a fluid-conveying pipe composed of two different materials," *International Journal of Engineering Science*, vol. 73, pp. 67-76, 2013.